



Contents lists available at ScienceDirect

Methods

journal homepage: [www.elsevier.com/locate/ymeth](http://www.elsevier.com/locate/ymeth)

## Quantification of telomere features in tumor tissue sections by an automated 3D imaging-based workflow

Manuel Gunkel<sup>a,1</sup>, Inn Chung<sup>b,\*,1</sup>, Stefan Wörz<sup>c,1</sup>, Katharina I. Deeg<sup>b</sup>, Ronald Simon<sup>d</sup>, Guido Sauter<sup>d</sup>, David T.W. Jones<sup>e</sup>, Andrey Korshunov<sup>f</sup>, Karl Rohr<sup>c,\*</sup>, Holger Erfle<sup>a,\*</sup>, Karsten Rippe<sup>b,\*</sup>

<sup>a</sup> VIROQUANT CellNetworks RNAi Screening Facility and Research Group High-Content Analysis of the Cell (HiCell), Bioquant Center, University of Heidelberg, Germany

<sup>b</sup> Research Group Genome Organization & Function, German Cancer Research Center (DKFZ) and Bioquant Center, Germany

<sup>c</sup> Department of Bioinformatics and Functional Genomics, Biomedical Computer Vision Group, Bioquant Center and IPMB, University of Heidelberg and German Cancer Research Center (DKFZ), Germany

<sup>d</sup> Department of Pathology, University Medical Center Hamburg-Eppendorf, Germany

<sup>e</sup> Division of Pediatric Neurooncology, German Cancer Research Center (DKFZ), Germany

<sup>f</sup> Department of Neuropathology, Heidelberg University Hospital, Germany

### ARTICLE INFO

#### Article history:

Received 11 May 2016

Received in revised form 26 September 2016

Accepted 27 September 2016

Available online xxxxx

#### Keywords:

Fluorescence microscopy  
Image analysis  
Alternative lengthening of telomeres  
FFPE tissue  
Glioblastoma  
Prostate cancer

### ABSTRACT

The microscopic analysis of telomere features provides a wealth of information on the mechanism by which tumor cells maintain their unlimited proliferative potential. Accordingly, the analysis of telomeres in tissue sections of patient tumor samples can be exploited to obtain diagnostic information and to define tumor subgroups. In many instances, however, analysis of the image data is conducted by manual inspection of 2D images at relatively low resolution for only a small part of the sample. As the telomere feature signal distribution is frequently heterogeneous, this approach is prone to a biased selection of the information present in the image and lacks subcellular details. Here we address these issues by using an automated high-resolution imaging and analysis workflow that quantifies individual telomere features on tissue sections for a large number of cells. The approach is particularly suited to assess telomere heterogeneity and low abundant cellular subpopulations with distinct telomere characteristics in a reproducible manner. It comprises the integration of multi-color fluorescence *in situ* hybridization, immunofluorescence and DNA staining with targeted automated 3D fluorescence microscopy and image analysis. We apply our method to telomeres in glioblastoma and prostate cancer samples, and describe how the imaging data can be used to derive statistically reliable information on telomere length distribution or colocalization with PML nuclear bodies. We anticipate that relating this approach to clinical outcome data will prove to be valuable for pretherapeutic patient stratification.

© 2016 Elsevier Inc. All rights reserved.

### 1. Introduction

Telomeres are the ends of linear chromosomes and in humans consist of the repetitive sequence 5'-TTAGGG-3' that is bound by

*Abbreviations:* 3D-TIM, 3D Targeted Imaging; ALT, alternative lengthening of telomeres; APB, ALT-associated PML-NB; CLSM, confocal laser scanning fluorescence microscopy; ECTR, extrachromosomal telomeric repeat; FFPE, formalin-fixed, paraffin-embedded; FISH, fluorescence *in situ* hybridization; IF, immunofluorescence; pedGBM, pediatric glioblastoma; PML, promyelocytic leukemia; PML-NB, PML nuclear body; PNA, peptide nucleic acid; ROI, region of interest; TMA, tissue microarray; TMM, telomere maintenance mechanism; SMLM, single molecule localization microscopy.

\* Corresponding authors.

*E-mail addresses:* [i.chung@dkfz.de](mailto:i.chung@dkfz.de) (I. Chung), [k.rohr@dkfz.de](mailto:k.rohr@dkfz.de) (K. Rohr), [holger.erfle@bioquant.uni-heidelberg.de](mailto:holger.erfle@bioquant.uni-heidelberg.de) (H. Erfle), [karsten.rippe@dkfz.de](mailto:karsten.rippe@dkfz.de) (K. Rippe).

<sup>1</sup> Shared first authors.

the shelterin protein complex [1]. These repeats and the bound proteins are critical for cells, since they prevent the DNA damage signaling machinery from recognizing chromosome ends as double-strand breaks. With every round of replication, however, the number of telomeric repeats decreases. Once the telomere length reaches a critical limit the cells either enter a state called replicative senescence or go into apoptosis. Hence, the continuous shortening of telomeres presents an effective control mechanism to restrict a cell's potential to divide. In order to proliferate indefinitely, cancer cells have to circumvent this control point by acquiring a telomere maintenance mechanism (TMM) to extend their telomeres. In most tumors, the enzyme telomerase that catalyzes the *de novo* synthesis of telomeric sequences is reactivated. In addition to the deregulation of several hundred genes that have been associated with aberrant telomerase activity, de-repression of

<http://dx.doi.org/10.1016/j.ymeth.2016.09.014>

1046-2023/© 2016 Elsevier Inc. All rights reserved.

telomerase can also be caused by mutations in the promoter of the telomerase gene *TERT* as well as structural rearrangements of *TERT* enhancers [2–4]. Apart from the various telomerase related pathways in cancer, alternative lengthening of telomeres (ALT) mechanisms exist in 25–60% of sarcomas, 5–15% of carcinomas and ~25% of glioblastomas (GBMs) [5–7]. These operate in the absence of telomerase and are based on DNA recombination and repair processes. ALT has repressed telomerase gene expression as an overarching characteristic feature and is typically associated with (i) heterogeneous telomere length distribution within individual cells and across tumor cell populations [8], (ii) formation of ALT-associated promyelocytic leukemia (PML) nuclear bodies (APBs) [9–11] that have PML protein in a spherical shell like structure assembled around the telomere repeats [12], (iii) mutations in genes like *ATRX* and *TP53* as shown for cell lines [13] and through deep-sequencing studies in GBMs, pancreatic neuroendocrine tumors and in other cancers [5,14,15], (iv) extrachromosomal telomeric repeats (ECTRs) [16,17], (v) variant telomeric repeat sequences [18] as well as (vi) high levels of the non-coding telomeric RNA transcript TERRA [19–21].

Notably, the TMM type can define distinct tumor subgroups that have been linked to patient subgroups and clinical parameters in several entities [3,4,22–25]. Thus, understanding telomere maintenance networks provides highly valuable and unique information about the cancer disease state that can be exploited for patient stratification and targeted therapies. This creates the need for methods to identify telomere features and TMMs from primary tumor samples. Often such samples are only available as formalin-fixed, paraffin-embedded (FFPE) tissue sections. These sections are collected either as individual samples or in the form of tissue microarrays (TMAs), where several hundred patient samples are combined on a single microscopy slide. The main method for detection of telomeres on these tissue sections is fluorescence *in situ* hybridization (FISH) with peptide nucleic acid (PNA) probes that recognize the telomeric repeat sequence 5'-TTAGGG-3' [26–28]. Once these probes reach the inside of the nucleus they hybridize with the complementary DNA strand with high affinity. The intensity of the fluorescently labeled telomere probe is proportional to the telomere repeat length. Frequently, telomere FISH analysis is used to identify ALT positive tumors. This application is based on the observation that so-called ultra-bright telomere foci of sizes in the range of several  $\mu\text{m}$  show a high correlation with the presence of ALT [5,29]. To this end, telomere FISH-stained tumor sections are manually inspected for the occurrence of FISH signals that are abnormally large and bright. However, it should be noted that the biological source of these ultra-bright foci is unclear. In addition, the current standard analysis uses 2D wide-field microscopy images and lacks structural information along the optical z-axis. Accordingly, in most studies tumor sections are classified only in a qualitative or semi-quantitative manner such as 'short' and 'long' telomeres. Such semi-quantitative analyses have been used to identify correlations between telomere length, tumor recurrences and patient survival in several cancer types including prostate cancer, breast cancer and neuroblastoma [27,30–32]. In other studies quantitative telomere FISH has been applied [33]. However, these previous studies do not exploit the increased accuracy of quantifying subcellular structures like telomeres from confocal image stacks and lack automated image analysis approaches, which makes it difficult to extend them to a larger number of samples.

In our previous work we have introduced a platform for a 3D imaging-based quantitative analysis of telomere features by confocal laser scanning fluorescence microscopy (CLSM) [34,35]. In these two studies an automated three-color confocal RNAi screening platform was developed that allowed us to analyze telomeres and colocalizations between telomeres and PML nuclear bodies

(PML-NBs) in cell lines to investigate the ALT mechanism. Based on image analysis the effect of RNAi-mediated knockdown of specific genes on the number and size of telomeres, PML-NBs, and APBs for each individual cell was determined. These features were also related to the cell cycle state as determined by DNA content measured using DAPI staining. Both the image acquisition and data analysis evaluated telomere features in three dimensions. As an extension of this previous work, we here describe an integrated approach to automatically quantify these telomere features on tumor tissue sections and TMAs and illustrate its application to pediatric glioblastoma (pedGBM) and prostate cancer samples. The workflow comprises three main parts: (i) An optimized protocol for fluorescence labeling of tissue sections. (ii) A combination of 2D imaging with a wide-field setup and high-resolution multicolor 3D confocal fluorescence microscopy termed 3D-TIM for 3D Targeted Imaging. An additional zoom-in step by single molecule localization super-resolution microscopy can be included that provides an additional ~10-fold improvement of the resolution. (iii) Quantitative high-resolution 3D image analysis of telomere features to yield statistically reliable measurements for primary tumor samples. The resulting data can be related to clinical data and provide information for pretherapeutic patient stratification.

## 2. Material and methods

### 2.1. Preparation of tissue sections

In the present work two types of samples were used, namely tissue sections from pediatric glioblastoma samples and prostate cancer TMAs. FFPE sections (5  $\mu\text{m}$  thickness) were prepared in the standard manner from pediatric glioblastoma tissue blocks. Tissues were assessed for tumor cellularity prior to selection to ensure the presence of >70% tumor cells. The TMA manufacturing process for the prostate cancer samples studied here was as described in detail previously [36].

### 2.2. PNA FISH on prostate cancer TMA

Prostate cancer tissue microarrays were deparaffinized by incubating them three times in xylene for 10 min, incubated twice in 96% ethanol for 5 min and dried at 48 °C for 3 min. Hybridization efficiency of the telomere repeat probe was improved for these samples by including a proteinase K treatment with 1 mg/ml proteinase K in TBS for 4 h at 37 °C. TMAs were washed twice with H<sub>2</sub>O for 3 min, briefly immersed in 96% ethanol and air dried for a few minutes. Denaturation and FISH probe hybridization was performed as follows: PNA-Hyb solution (70% formamide, 10 mM Tris HCl, pH 7.5, 0.1  $\mu\text{g}/\text{ml}$  salmon sperm) containing 0.1  $\mu\text{M}$  of a Cy3-labeled telomere probe (CCCTAA)<sub>3</sub> (TelC-Cy3, Panagene) and of a FAM-labeled PNA probe (ATTTCGTTGGAAACGGGA) that is directed against the CENP-B binding site in the centromeric alpha satellite DNA (CENP-B-FAM, PNA Bio) was added to the TMA, the slide was heated to 80 °C for 5 min for denaturation and hybridization took place at RT in a wet chamber. Next, the TMAs were washed twice for 15 min in PNA wash buffer (70% formamide, 10 mM Tris-HCl, pH 7.5), 1 min in 2 $\times$  SSC, 5 min in 0.1 $\times$  SSC at 55 °C, 2  $\times$  5 min in 0.05% Tween-20/ 2 $\times$  SSC and three times in PBS for 5 min. After incubation in 70%, 85%, and 100% ethanol, the slide was air dried and mounted with Prolong reagent including DAPI.

### 2.3. PNA FISH and immunofluorescence on FFPE pedGBM tissue sections

Combined FISH and immunofluorescence was essentially carried out as described in Ref. [28]. Paraffin was removed from the

tissue slices of 5  $\mu\text{m}$  thickness by melting at 65  $^{\circ}\text{C}$  and washing the slides in xylene. After hydration through a graded ethanol series, slides were incubated in 1% Tween-20 for 1 min before antigen unmasking, for which the slides were placed in 10 mM sodium citrate buffer (pH 6), boiled at 700 W in a microwave, and left at 120 W for another 9 min. After cooling down, incubation in increasing ethanol series and a short period of air-drying, the hybridization with the PNA FISH probes was performed. For this, tissue sections were incubated with 0.1  $\mu\text{M}$  of a Cy3-labeled telomere probe (CCCTAA)<sub>3</sub> (TelC-Cy3, Panagene). In experiments where the centromeres were also visualized 0.1  $\mu\text{M}$  of the FAM-labeled CENP-B PNA probe (ATTCGTTGGAAACGGGA) was added at the same time. The hybridization took place in 70% formamide, 10 mM Tris-HCl, pH 7.5, 0.1  $\mu\text{g}/\text{ml}$  salmon sperm. First, slides were denatured at 84  $^{\circ}\text{C}$  for 5 min and then left overnight at room temperature in a wet chamber for hybridization. Next, slides were washed three times for 15 min in PNA wash buffer, followed by three 5 min-washes in PBST. Then the sections were incubated with an anti-PML antibody (1:100, PG-M3, sc-966, Santa Cruz) in PBS overnight at 4  $^{\circ}\text{C}$  in a wet chamber. Finally, they were washed with PBST, incubated with the secondary antibody (here: anti-mouse IgG coupled to Alexa647, Life Technologies) for 1 h at RT, again washed with PBST and embedded with Prolong including DAPI. Here, the immunofluorescence step is performed after the FISH probe incubation, but we note that some other laboratories use a different order, which works as well.

#### 2.4. Image acquisition

A detailed description of the targeted image acquisition procedure is provided as [supplementary protocol 1 in the Supplementary Information](#). Wide-field images were acquired with a fully automated Olympus IX81 ScanR screening microscope. A magnification of 10 $\times$  (Olympus UPlanSApo, NA 0.4) was chosen, resulting in a field of view of 866  $\mu\text{m} \times 660 \mu\text{m}$ . The sample was illuminated with a 150 W Hg/Xe mixed gas arc burner in combination with appropriate filter combinations for DAPI and Cy3, respectively. For the TMAs, 725 (29  $\times$  25) adjacent fields of view were recorded for cell selection, with overlapping areas of 30  $\mu\text{m}$  in x- and y-direction in order to enable automatic image stitching. In total an area of  $\sim 3.8 \text{ cm}^2$  was imaged. For confocal imaging a Leica TCS SP5 point scanning confocal microscope with additional MatrixScanner software was used. In all cases, a 63 $\times$  objective lens (Leica HCX PL APO, NA 1.40) was employed. Scan speed, pixel size, field of view, z-stacks and channels were set for each sample appropriately; typical values for high-resolved imaging of previously identified regions of interest (ROIs) were 200 Hz scan speed, 96 nm pixel size at a field of view of 256  $\times$  256 pixels, 41 axial layers at 250 nm spacing and 3 color channels with 2 $\times$  frame averaging. Single molecule localization microscopy (SMLM) was performed with the same Leica TCS SP5 microscope used for confocal imaging, equipped with an additional wide-field unit. For illumination, a 647 nm diode laser with 140 mW maximum power (Luxx, Omicron, Rodgau-Dudenhofen, Germany) and a 561 nm solid state laser with 156 mW maximum power (Jive, Cobolt, Solna, Sweden) were used. The laser beam path was additionally coupled into the microscope through the back illumination port by a switchable mirror. Highly inclined and laminated optical sheet (HILO) illumination of the sample was controlled with an adjustable mirror. Images were recorded by an sCMOS camera (Hamamatsu Orca Flash 4.0) at 10 ms integration time and 5000 frames per dataset with each maximum laser power in order to induce photoswitching. From the total field of view of 2048  $\times$  2048, a sub-region of 200  $\times$  200 pixel (20  $\times$  20  $\mu\text{m}^2$ ) was acquired. Prior to SMLM imaging, a wide-field image was acquired at low laser intensities. The area illuminated by high laser power was restricted to the target

cell by an adaptable aperture in the illumination beam path in order to protect surrounding structures from photobleaching. SMLM datasets were reconstructed using the ImageJ plugin ThunderSTORM [37].

#### 2.5. 3D image analysis

To adapt our previous work on the automatic extraction of telomere features from cell line samples to tissue sections, an advanced 3D model-based image analysis approach was developed. It accounts for the elevated levels of tissue sample heterogeneity, image artifacts and significant background levels (Fig. 4A) [35,38]. The approach supports multiple microscopy channels, where depending on the experiment a maximum of four 3D channels was used (i.e., centromeres, telomeres, PML-NBs, and DAPI staining). To overcome artifacts caused by false positive segmentation such as autofluorescent erythrocytes (Fig. 4E), first a 3D artifact detection and segmentation step is performed. Artifacts were determined in the telomere channel and segmented in 3D by performing noise reduction (3D Gaussian filter) followed by automatic thresholding (intermodes scheme), different morphological operations, and object filters. The inverted binary segmentation result was used as a mask for subsequent segmentation of the cell nuclei in the DAPI channel. For the 3D segmentation of the cell nuclei an approach similar to Ref. [35] was used. It is based on different automatic thresholding schemes (e.g., Otsu, entropy-based) where the artifact mask was included. The nuclei segmentation result defines a mask for the analysis of all other channels, and it serves for normalization of analysis results with respect to the volume of the cell nuclei. Depending on the experiment, a further labeling step was carried out to enable a cell-based analysis.

For automatic quantification of relevant spots in the telomere, PML and centromere channels, a series of 3D spot detection, 3D model-based segmentation, and spot filtering was performed. To automatically detect spot candidates, different image analysis operations were applied to the 3D image data to obtain (coarse) center positions of the spots: for noise reduction we used either a 3D Gaussian filter or a 3D Laplacian of Gaussian filter. For suppressing the image background all intensity values below a certain threshold value, which was automatically computed for each image from the image histogram based on the region of the cell nuclei [38], were clipped. Finally, we performed a local maxima search within cubic 3D ROIs, where the local maxima represent the spot candidates. In the second step, each detected spot candidate was quantified based on 3D least-squares model fitting using a 3D Gaussian parametric intensity model. A 3D Gaussian model well represents the 3D intensity profile of the considered spots. The model reads

$$g_{M,Gaussian3D}(\mathbf{x}, \mathbf{p}) = a_0 + (a_1 - a_0)g_{Gaussian3D}(\mathcal{R}(\mathbf{x}, \alpha, x_0), \sigma_x \sigma_y \sigma_z).$$

where  $\mathbf{x}$  is a 3D position,  $\mathcal{R}(\mathbf{x}, \alpha, x_0)$  a 3D rigid transform,  $a_0$  and  $a_1$  denote the local background and peak intensity levels, respectively, and  $\sigma_x$ ,  $\sigma_y$ , and  $\sigma_z$  are the standard deviations that represent the three semi-axes describing the ellipsoidal shape of the spots. A detailed description of the 3D model-based image analysis is provided as [supplementary protocol 2 in the Supplementary Information](#) and in Ref. [38]. By fitting parametric intensity models that describe the 3D intensity profiles by anisotropic 3D Gaussian function a subvoxel resolution of the model parameters including the 3D position and semi-axes is obtained without the need for additional deconvolution of the image. To enable accurate and robust fitting of the variably sized telomere spots, the size of the 3D ROI used for model fitting was automatically determined for each spot by a multiscale scheme similar to that described in Ref. [39] (Fig. 4B–D). Here the spot size is coarsely determined by analyzing the results

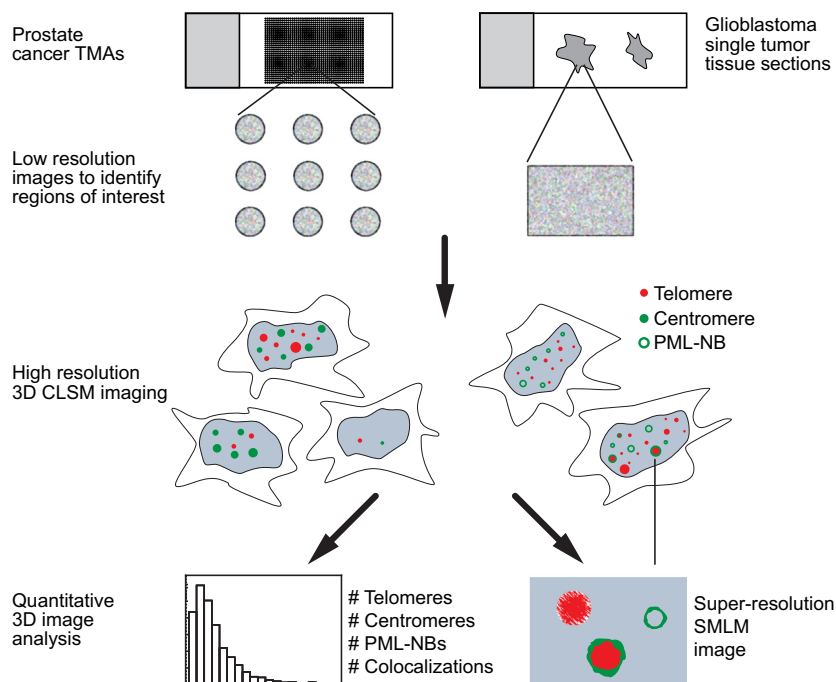


**Fig. 1.** Schematic overview of workflow. The 3D imaging and analysis of FFPE tumor tissues either on TMAs or as single sample sections consists of three main parts: sample staining, image acquisition, and image analysis. These steps are illustrated in detail in Figs. 2–4. Briefly, the fluorescence labeling comprises FISH of telomeric and centromeric repeat sequences, immunofluorescence of PML protein and counterstaining of the DNA with DAPI. The image acquisition involves a combination of 2D imaging with a wide-field setup followed by targeted CLSM imaging with an optional zoom-in step by super-resolution microscopy (SMLM). In the 3D image analysis, subnuclear structures are identified from 3D spot detection to quantify number, size, signal intensity, and co-occurrence of telomeres, centromeres, and PML-NBs. In this manner, crucial information on the active TMM in a given tumor sample is obtained.

of a 3D Hessian-based blob detector at different image scales. In contrast to the scheme in Ref. [39], which has been designed for larger spots of irregular shape, we here account for the heterogeneous spot sizes by adapting the detector response. Finally, based on the quantified model parameters, different spot filters were applied to the fitting results to exclude invalid spots, e.g. those that significantly deviate from a typical spot regarding their shape or size or that displayed a low image contrast as they likely represent noise. Since the image statistics vary among different images, a threshold for the contrast based on the image histogram in the region of a spot was computed. For calculating the integrated intensity of each fitted spot, an analytic formula was derived that integrates the intensities of the 3D Gaussian model over the ellipsoidal volume as described in detail in the [Supplementary Information](#). The analytic solution of the triple integral reads

$$\text{Integrated intensity} = \frac{3a \text{vol}(\sqrt{2e\pi}\text{erf}(1/\sqrt{2}) - 2)}{2\sqrt{e}}$$

where  $a = (a_1 - a_0)$  denotes the spot contrast,  $\text{vol} = \sigma_x\sigma_y\sigma_z4\pi/3$  is the ellipsoidal volume of the spot, and erf denotes the error function. The integrated intensity is computed from the fitted model parameters, i.e., the noisy image intensity values were *not* directly used.

To determine cell-based co-occurrences as well as 3D colocalizations the results of pairs of spot channels were combined. The accessibility of the PNA FISH probes (see Section 3.2, Fig. 2B) can be assessed with a 3D cell-based co-occurrence analysis that quantifies the number of centromeres and telomeres per cell nucleus. For the quantification of colocalizations between telomeres and PML-NBs the 3D spot geometries were obtained with subvoxel accuracy from model fitting. These data were subsequently used to determine the spatial overlap in 3D of the two spots from different channels and the degree of colocalization [35] (Fig. 4F, G).

Finally, results of all channels and analysis steps are combined and all results for each single sample were summarized and further statistics computed. The telomere length distribution was quantified for each sample based on the histogram of the integrated intensities of all telomere spots, and normalized with respect to the volume of DAPI staining.

For each experiment the same set of parameters was applied and all images were analyzed in batch mode (running twelve jobs in parallel). The computation time for a single multichannel 3D image was about 30–40 s, and a full TMA required about 1 h on an Intel Xeon CPU with 2.67 GHz running Linux. For the example shown here a total 2583 multichannel 3D images from prostate cancer TMAs and 247 such images from several pedGBM sections were evaluated.

### 3. Results and discussion

#### 3.1. An integrated workflow for the automated fluorescence microscopy and analysis of telomere features in primary FFPE tumor tissue sections

The overall approach for the 3D imaging of FFPE tumor tissues described here is illustrated in Fig. 1. It consists of three technically challenging parts. The first part involves the multi-color staining of the samples with three types of staining that are informative for the TMM analysis: (i) FISH of telomeres to identify their number and length distribution. In addition, FISH staining of centromeres provides a valuable control. It indicates whether the absence of a telomere FISH signal indeed reflects very short telomeres or simply the failure to hybridize the probe in a certain part of an image. (ii) Immunofluorescence (IF) of PML protein, which can be evaluated in terms of its colocalization with telomeres as a marker for ALT. (iii) Counterstaining of the DNA with DAPI to identify nuclei.

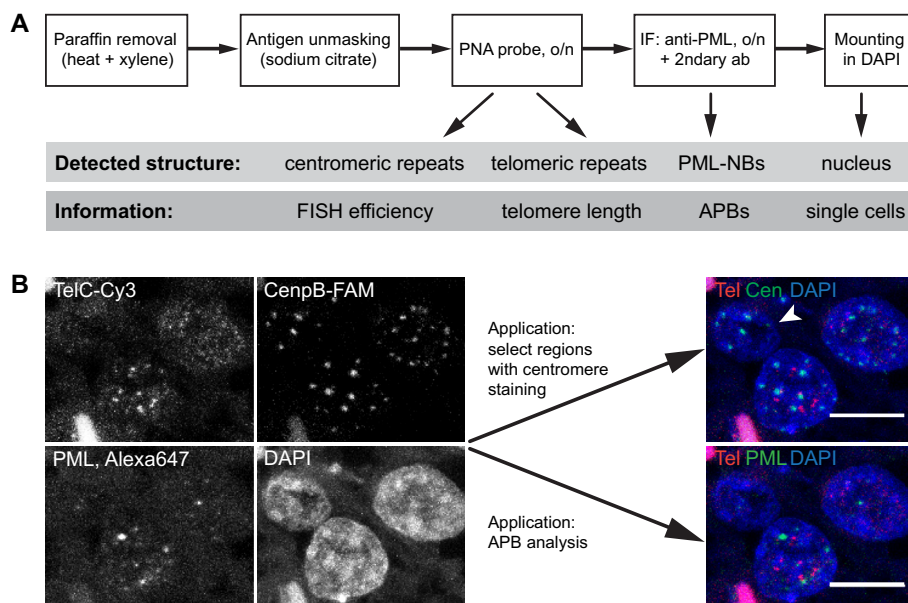


**Fig. 2.** Staining of nuclear structures in FFPE sections. (A) Schematic workflow for the staining procedure of FFPE tissue sections to detect telomeric and centromeric repeats by PNA FISH probes as well as PML-NBs by immunofluorescence against the PML protein. Additionally, the nucleus is visualized by DAPI staining. The detection of these nuclear structures allows the discrimination of single cells and provides information about the efficiency of the FISH probe hybridization, the length of the telomeres, and the presence of APBs. (B) Representative CLSM image of a pedGBM tissue section that has been treated with PNA probes against the telomeric repeat sequence (labeled with Cy3) and against centromeric repeats (labeled with FAM) and additionally stained for PML protein (labeled with Alexa647). The nuclei are detected by DAPI. Two merged images are shown. The upper one shows a merge of the telomere (red), the centromere (green), and the DAPI (blue) signal. The arrow indicates a nucleus that was accessible for the FISH probes as is obvious from the detection of the centromeres but that did not display any signal from the telomere FISH probe. Accordingly, this cell can be classified as one with telomeres too short to be detected using telomere FISH as opposed to one not being accessible for the FISH probe. Below is a merged image of the telomere channel (red), the PML IF (green) and DAPI (blue). Using this combination the presence of APBs can be analyzed. All images are maximum projections. Scale bars, 10  $\mu$ m. (For interpretation of the references to colour in this figure legend, the reader is referred to the web version of this article.)

The second part of the workflow comprises the image acquisition: (i) First, the whole tissue sample is imaged in 2D with a wide-field setup. (ii) Images are analyzed on-the-fly to identify regions of interest (ROIs), e.g. nuclei showing DAPI and/or telomere signal. (iii) Information on the corresponding positions is fed back to the microscope. (iv) High-resolution multicolor confocal fluorescence 3D images are acquired for an in-depth automated analysis of subcellular structures at the regions of interest. (v) An optional zoom-in step by photoactivated localization microscopy can be applied for analyzing the structure of selected parts of the image at a resolution that is higher by an order of magnitude.

The third part of the workflow consists of an automated 3D image analysis: (i) A 3D artifact detection and segmentation step removes artifacts like autofluorescent signal from contaminating cells or debris. (ii) Regions of interest are selected via a 3D segmentation of the cell nuclei. (iii) Subnuclear structures are identified from 3D spot detection and quantification. (iv) A 3D cell-based co-occurrence analysis can be performed by analyzing the number of quantified centromeres and telomeres within each cell nucleus. (v) Via a 3D colocalization analysis, APBs are identified from co-occurring telomere and PML signals.

### 3.2. Combined immunofluorescence and FISH staining for detection of ALT positive tumors using confocal laser scanning microscopy

The majority of studies that analyses the TMM in FFPE tumor tissues applies telomere FISH alone to identify ALT activity. However, a few issues should be considered. Different fixation conditions used for different tumor samples as well as heterogeneous results within one tissue sample can make some areas on a slide more accessible for the PNA FISH probe than others. This is particularly important when comparing several tumor samples with respect to their telomere lengths. Usually, it is assumed that a sin-

gle sample or all the tissue cores on a given TMA slide have minimal technical variations since they are stained in the same manner. Thus, the lack of a telomeric signal would indicate the presence of only very short and thus undetectable telomeres. However, the absence of a telomere FISH signal could alternatively be due to the inaccessibility of this particular cell for the FISH probe. To control for this issue, a second PNA FISH probe can be applied [28]. For comparison this should also be directed against a repetitive sequence in the genome, such as centromeric repeats. The detection of a centromere FISH signal in a given cell indicates that technically the FISH probe can access this nucleus and a lack of telomere FISH signal would indeed be due to the presence of very short telomeres. If no centromere signal is observed, this will argue that none of the probes could access the nucleus. Accordingly, such a cell should be omitted from the analysis. Secondly, it is problematic to rely only on the telomere signal to identify a tissue as ALT positive. It is widely accepted that tumor cells and cell lines that use the ALT mechanism have a very heterogeneous telomere length distribution within a cell population and also within a single cell. However, in most telomere FISH studies on tissues the telomere length distribution is not determined but only the presence of ultra-bright foci is evaluated. These foci are used as an ALT marker despite the uncertainty about their biological source and function. Thus, for a more reliable characterization of a tissue section with respect to its TMM, the presence of APBs should be assessed. These nuclear subcompartments are specific for the vast majority of ALT positive cells [9]. By an automated quantification of telomere colocalizations with PML-NBs the number of APBs can be determined [34,35]. To our knowledge all primary tumor samples that have been analyzed with respect to these structures show an association between the presence of APBs and ALT. This refers to APBs as complexes of PML assembled around distinct telomeres [9] but not to the colocalization of PML with large ultra-bright telomere foci that

have dimensions of several  $\mu\text{m}$ . For the latter, a study on pancreatic neuroendocrine tumors reported that 39% of all tumors with ultra-bright foci indicative of ALT showed a colocalization of these ultra-bright telomere signals with PML [5]. Furthermore, it should be noted that telomerase negative bona fide ALT cell lines have been described that lack APBs [40–42]. Thus, it is conceivable that certain primary tumor samples have ALT but lack APBs.

To evaluate the presence of APBs we stained FFPE tissue sections of pedGBM samples with FISH PNA probes against telomeric and centromeric repeats as well as with IF against the PML protein. Images were acquired by CLSM and analyzed automatically with respect to the telomere length distribution and frequency of APBs. The workflow of the sample preparation is illustrated in Fig. 2A. Essentially a protocol similar to that given in Ref. [28] was used as described in Section 2.3. The detailed protocol has to be optimized for each tissue and antibody in terms of accessibility of telomeric DNA and antigen retrieval as critical parameters for the FISH and immunofluorescence signal. In particular, the antigen retrieval step and inclusion of an additional enzymatic treatment such as with proteinase K should be tested. As indicated in Fig. 2A, an appropriate combination of dyes allows the simultaneous detection of centromeres, telomeres, and PML-NBs in single cells. In Fig. 2B some representative CLSM images are shown. The combination of centromere and telomere signal is analyzed for quantifying the telomere length distribution in a given sample (Fig. 2B, top merge image). This combination of readouts is useful to assess the efficiency of the FISH probes and to evaluate whether the lack of a telomere signal is indeed due to the presence of very short telomeres or attributed to technical issues. Additionally, the telomere signal can be analyzed in relation to a PML-NB staining (Fig. 2B, bottom merge image). With this combination of stainings the frequency of APBs can be evaluated. From the number of APBs the TMM of tumor cells can be inferred as described below in further detail.

### 3.3. 3D Targeted Imaging

In order to identify, relocate and image ROIs within individual cores on a TMA, two routines have been implemented. The first one consists of a sequential mode where a prescreen of the sample at low resolution is followed by image analysis based target identification, revisiting of those targets and subsequent high-resolution 3D acquisition with additional color channels (Fig. 3A–C). The second routine uses on-the-fly switching of the optical configuration upon automatic identification of an ROI (Fig. 3D, E). In the first case, a complete TMA was scanned on an Olympus IX81 ScanR microscope with a magnification of 10x. Images were recorded in the DAPI color channel with an overlap of 30  $\mu\text{m}$  in x and y direction to ensure complete coverage and to enable stitching of adjacent images (Fig. 3C, left). The resulting images were processed using KNIME (Konstanz Information Miner, [www.knime.org](http://www.knime.org)) and the KNIME image processing plugins (KNIP) in order to extract structures that resemble cells. The complete workflows as well as a detailed description are provided in [supplementary protocol 1](#). As candidates for subsequent high-resolution multi-color 3D imaging, all objects with a minimum intensity and an area falling in an appropriate interval were considered. Due to the heterogeneity between individual cores of the TMA in intensity and shape of the cell nuclei, threshold levels for filtering were adopted based on the distribution of these features within the single cores. The global position for each ROI on the TMA was retrieved from the stage position of each image (image metadata) together with the position of the ROI within the respective image. A unique ID was assigned to each ROI as well as the coordinate of its associated spot based on the regular arrangement of the TMA, starting on the top left with (0|0). The corresponding KNIME

workflow is depicted in Fig. 3B (upper part). The sample was then transferred to a Leica TCS SP5 confocal microscope and a coordinate transfer of the ROIs from the wide-field to the confocal microscope was performed (Fig. 3B, lower part, see also [supplementary protocol 1](#)). At each ROI position, a confocal stack with three colors (Cy3-Telomere, FAM-Centromere, DAPI-nucleus) and 41 z-planes (distance 0.25  $\mu\text{m}$ ) was acquired (Fig. 3C, most right). Imaging of the whole TMA took about 30 min for the wide-field prescreen. For high-resolution 3D confocal imaging, each ROI was acquired in 2.5 min. On average 80 ROIs per core were imaged, resulting in 3.3 h imaging time per tissue core or around 70 days for a TMA with 500 cores.

For the second image acquisition routine, a TMA was scanned in 2D at medium resolution on a confocal Leica SP5 microscope using the Leica MatrixScreener software (Fig. 3F, left). This software provides a server-client interface (termed ‘computer aided microscopy’, CAM), by which the scan routine can be influenced and altered. The scan was embedded into a KNIME workflow loop (Fig. 3E). Special loop start and loop end nodes for addressing the CAM-interface have been developed in collaboration with KNIME and Leica. In each step of the loop, one scan field was imaged and directly processed within KNIME via the KNIME image processing plugins (KNIP). Cells were identified based on the DAPI staining, and single telomeric spots within these cells were counted based on the Cy3 signal. Nuclear structures containing five or more telomeric spots were considered as candidates for high-resolution 3D imaging. The positions of these candidates were collected and fed back to the microscope via the KNIME-CAM-interface. Upon receiving these positions, a second high-resolution 3D routine was started immediately at the microscope that acquired those candidates. Afterwards the next iteration of the loop was started and the next scan field was recorded. In 36 cores, 1303 ROIs have been identified with 69 h image acquisition time. A whole TMA with around 500 cores would thus be imaged in about 42 days, assuming the same average of 36 ROIs per core.

The first routine can be applied to any pair of microscopes. A prerequisite is the ability to read and write position information along with the images. It can also be performed on the same microscope system for prescreening and targeted imaging or even for targeted imaging if a set of images of a specific sample already exists and specific subregions are selected for higher resolution image acquisition. Subpopulations within the single cores can be identified and representatives of these populations can be acquired with higher resolution in 3D or additional color channels. Individual cores can be addressed by filtering for their coordinates in the position list given to the microscope. The decision, which ROIs to select for high-resolution 3D imaging, can be based on the complete wide-field dataset of the whole TMA.

If the phenotype of the structures to be acquired is known beforehand, the second routine can be used. The microscope then acts as a trigger system, which can switch the acquisition mode upon registration of a predefined event (detection of a structure of interest, rare cell cycle event, etc.), acquires images of the desired resolution, and afterwards continues the screen.

The time needed for imaging with a single point confocal system becomes prohibitive for a larger number of samples. Based on our preliminary tests this issue can be addressed by applying 3D-TIM on a spinning disk microscope like the PerkinElmer Opera system. The field of view is fixed on this system to approximately 150  $\mu\text{m}$   $\times$  100  $\mu\text{m}$  with 60 $\times$  magnification and a whole 3-color 3D stack can be acquired in 1.5 min. Within each field of view multiple cells within the tissue are imaged at once. If 5–10 of these regions per core are automatically selected for imaging by TIM, 500 cores could require 60–120 h or 2.5–5 days imaging time, i.e. a roughly tenfold speed increase can be obtained.

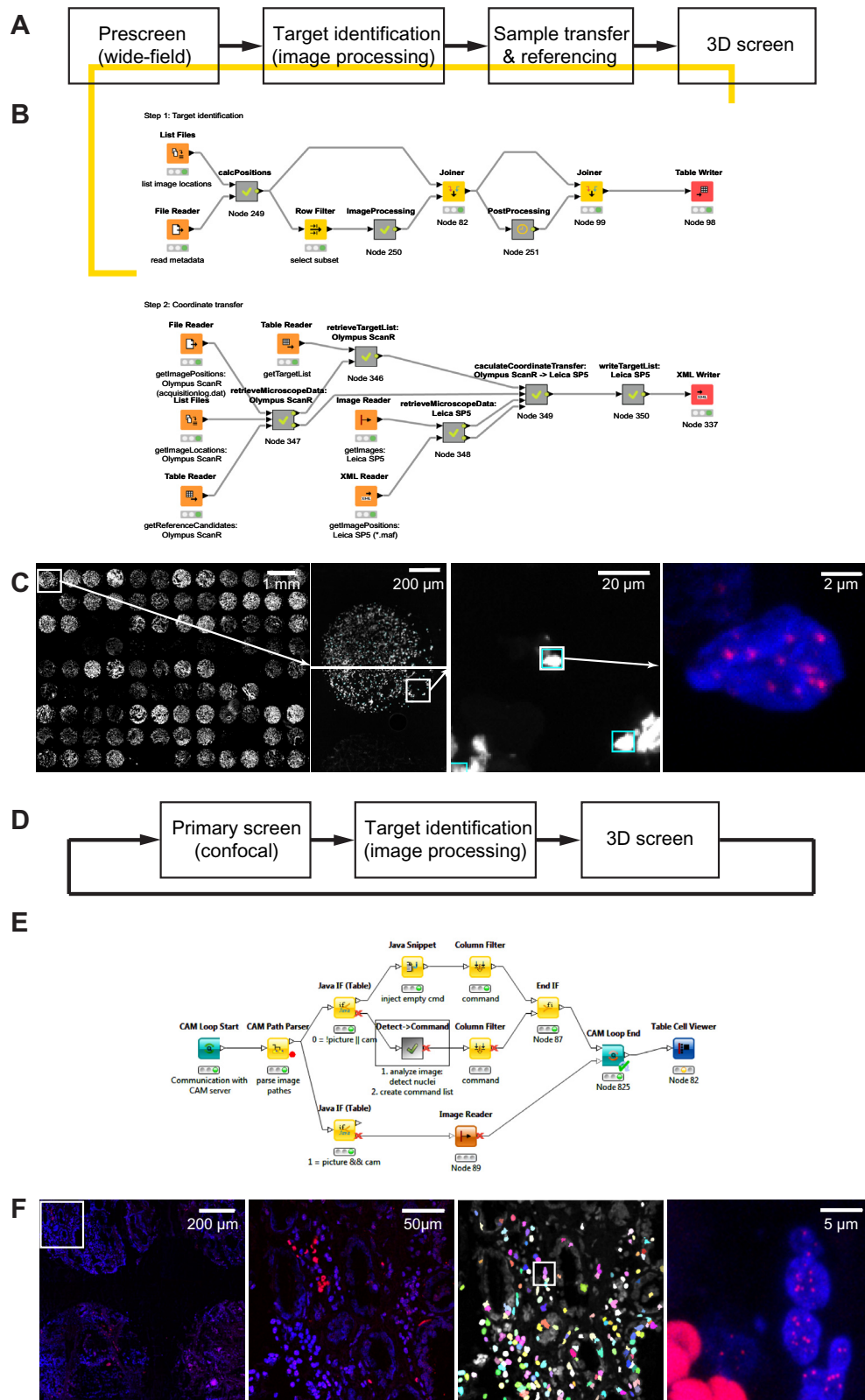


**Fig. 3.** 3D Targeted Imaging (3D-TIM). (A) Schematic workflow for sequential imaging on different scales. First, ROIs are identified in a pre-screen. Then, the sample is transferred to a second microscope and after a referencing step the previously identified regions can be addressed and acquired in 3D with higher resolution and more color channels. (B) KNIME implementation of the workflow in A. (C) Example images. On the left, the single tissue spots of a TMA can be seen. Next to it, the two wide-field images acquired of the first spot are shown. These were processed in order to identify the ROIs as described in the text. On the right side, the same region is shown as imaged by CLSM after sample transfer and referencing (maximum projection of 41 axial layers). (D) Schematic workflow for integrated imaging on different scales. In each image of a primary screen, ROIs are identified. These positions are directly fed back to the microscope and a high-resolution z-stack is acquired for each region. Afterwards, the next scan field of the primary screen is acquired. (E) KNIME implementation of the workflow in D. (F) Example images. On the left, the single spots of a TMA can be seen. Next to it, a two-color image of the highlighted region of the confocal prescreen is shown. This image is directly processed in order to find ROIs (i.e. cellular structures comprising five or more telomere spots) indicated in random colors. On the right side, one region is shown as imaged by the subsequent 3D screen (maximum projection of 41 axial layers).

### 3.4. Extraction of telomere features from fixed tumor sections via automated 3D image analysis

To extract telomere features from fixed tumor sections, a robust 3D model-based image analysis approach described in detail in Section 2.5 was developed (Fig. 4). This approach includes an

artifact detection step to exclude regions of artifacts from further analysis (e.g. fragments of red blood cells), a cell segmentation step, and 3D model-based spot quantification. The approach is fully automated without the need of manual parameter adjustments for individual images. For the application shown here, three fixed sets of parameters were used: one for the analysis of tissue spots from

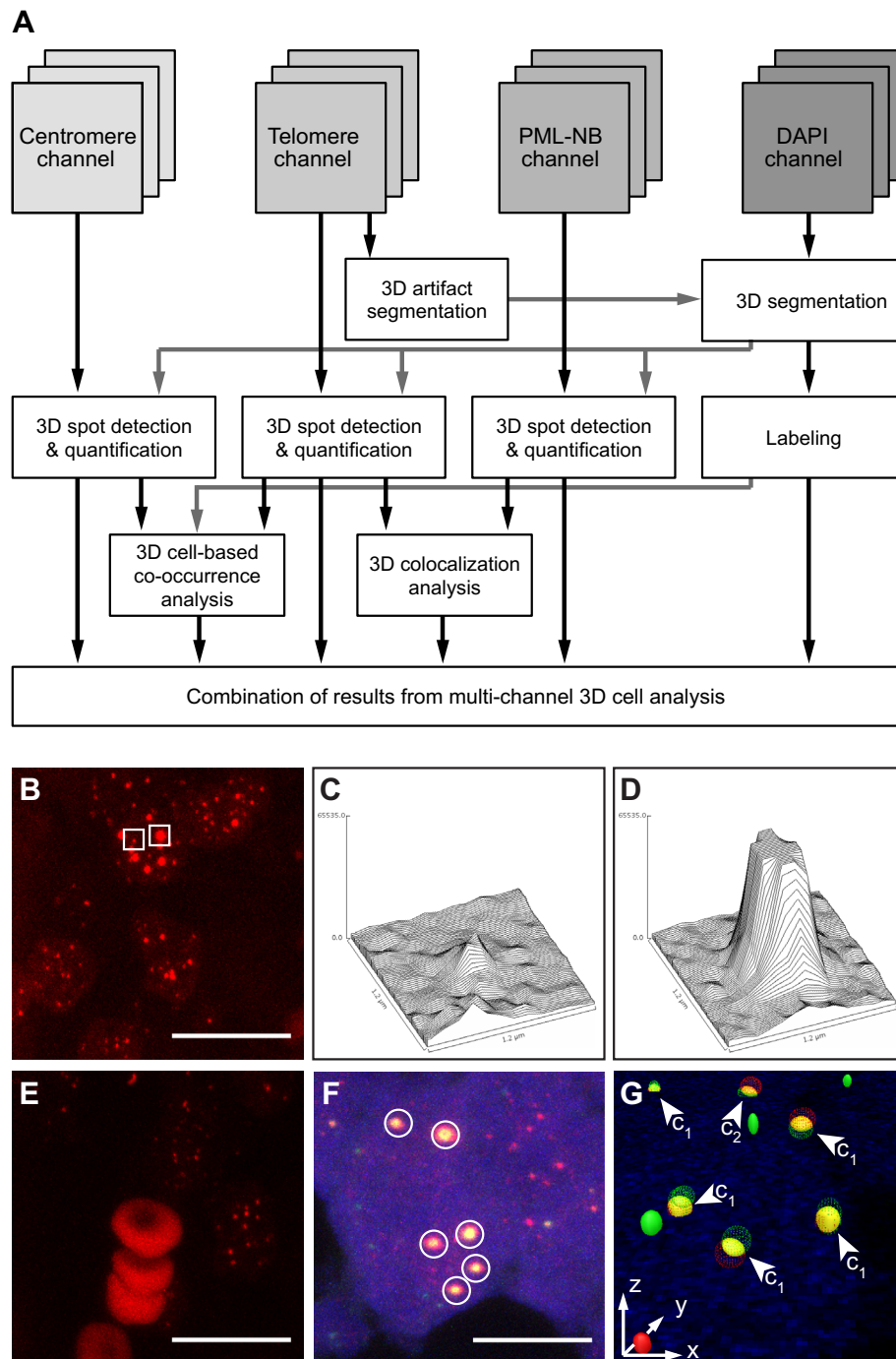


**Fig. 4.** Automated 3D image analysis of telomere features from tissues. (A) Schematic workflow for 3D quantitative image analysis of 3D multichannel microscopy images. Subnuclear structures are identified using 3D spot detection after 3D segmentation of DAPI stained regions in the different color channels. The number, size and signal intensity of telomeres, centromeres and PML-NBs are quantified using a 3D model-based approach. Finally, 3D cell-based co-occurrence and colocalization analyses are conducted. (B) Example image of the telomere channel from imaging a prostate cancer TMA showing telomere spots of heterogeneous sizes. (C, D) 2D intensity plots of a small telomere spot (C) and a telomere spot with high intensity (D) (both highlighted in B). (E) Example image of the telomere channel from the TMA image acquisition depicting large artifacts (erythrocytes). (F) Overlay of telomere, PML, and DAPI channels of a pedGBM sample, where six colocalizations of PML-NBs with large telomeres are highlighted. (G) 3D visualization of the quantified geometry of the telomeres, PML-NBs, and colocalizations for the image in F with marked colocalization classes  $c_1$  and  $c_2$ . Images in B, E, and F are maximum intensity projections. Scale bars, 10  $\mu\text{m}$ . (For interpretation of the references to colour in this figure legend, the reader is referred to the web version of this article.)



TMA of prostate cancer and two for the analysis of pedGBM tissues. Common parameter settings for all images included the chosen parametric model for spot quantification (anisotropic 3D Gaussian intensity model), the initial model parameters, the range of 3D ROI sizes used for model fitting (radii of 3–10 voxels), and the 3D ROI size for local maxima search ( $5 \times 5 \times 5$  voxels). In contrast, the parameter settings for 3D spot detection, spot filters, and 3D DAPI segmentation were adapted to the intensity distribution obtained for the staining of a given TMA or tissue sample. For the spot detection in the TMA images, a 3D Gaussian filter with isotropic smoothing ( $\sigma = 1$  voxel) was used for noise reduction followed by intensity clipping using relative factors of  $c = 2$  for telomeres and  $c = 4$  for centromeres (see [38] for details). In the images from the pedGBM sections, a 3D Laplacian of Gaussian filter with anisotropic smoothing ( $\sigma_{x,y} = 1.5$  and  $\sigma_z = 1$  voxels) was used as well as relative factors of  $c = 14$  or  $c = 16$  for telomeres, centromeres, and PML-NBs. Furthermore, spots were filtered using the minimum spot contrast with relative factors of  $s = 2$  (prostate cancer images) and  $s = 3$  or  $s = 4$  (glioblastoma images) with respect to the standard deviation of the image histogram. In order to segment the DAPI signals Otsu thresholding was employed with one threshold (TMA images) as well as Otsu thresholding with two thresholds or maximum entropy thresholding (pedGBM images).

As an example, Fig. 4G shows a 3D visualization of the 3D segmentation results of telomeres (red) and PML-NBs (green) of one multichannel microscopy image of the glioblastoma sample shown in Fig. 4F. In our approach a 3D geometric description of the telomere and PML-NBs spots is obtained. From this parameterization, colocalizations between these spots are detected and classified automatically (Fig. 4G). Two different classes of colocalizations were defined: In class 1 (c1) the center of one spot lies within the other spot. The class 2 (c2) colocalization is a less stringent definition that only requires an overlap of the spots. Note that with standard approaches, colocalizations are usually determined based on color overlays of the red and green channels (see discussion in Ref. [38]). Such color overlays strongly depend on the image contrast and background signal in the different channels. They were not applicable for the tissue samples due to the high heterogeneity of intensity variations and image artifacts. In contrast, by using a 3D geometry-based approach colocalizations could be determined robustly in the presence of image contrast variations.

### 3.5. 3D-TIM of telomeres on a prostate cancer TMA reveals differences in the telomere length distribution between tissue cores

In order to illustrate the automated image acquisition and analysis we evaluated 45 prostate cancer tumor sections on TMAs with respect to their telomere signals detected with a Cy3-labeled FISH probe. To demonstrate the variety of results that were obtained from this, we show here the telomere length distributions of four representative tissue cores from the TMA (Fig. 5). The amount of hybridized telomere probe is directly proportional to the number of telomeric repeats and hence the signal intensity is a direct indication of the telomere length. The distribution of the telomere intensities from different prostate cancer biopsies revealed the heterogeneity of the telomere length distribution between tissue spots. For example, the maxima of the distribution for II and III were shifted towards longer telomeres as compared to I and IV, which had the highest frequency at the lowest intensity bin (Fig. 5). In addition, samples III and IV had higher fractions of very long telomeres than I and II. This type of quantitative information cannot be obtained from the commonly performed manual examination of wide-field images. The comparison of the frequencies of telomere intensities on a cell-to-cell basis between different tissues requires an automated segmentation of individual DAPI stained nuclei in FFPE tissues. This step is technically challenging as nuclei in very close vicinity often cannot be well separated from each other due to low image contrast and significant background signal. To overcome this problem, normalization to a measured DAPI volume has been implemented (Fig. 5B). Currently, one caveat here are relatively high background DAPI signals in some of the tissue sections. One example is depicted in histogram IV where an abnormally high DAPI volume was measured. In order to address this issue the ratio of the centromere FISH to DAPI signal can be determined ( $\#centro/1000 \mu m^3$  in Fig. 5). A low value of this parameter is indicative of technical problems in the region evaluated: Either the measured DAPI signal has an unusually high background or the FISH probe hybridization was not efficient on this particular tissue spot. It is advantageous to conduct this analysis with the centromere probe. The number of centromeres per nuclei should reflect the chromosome content of the cell, whereas the detection of telomere signals is affected by the telomere maintenance mechanism and cell proliferation. Thus, a low centromere/DAPI ratio represents an informative quality parameter to identify

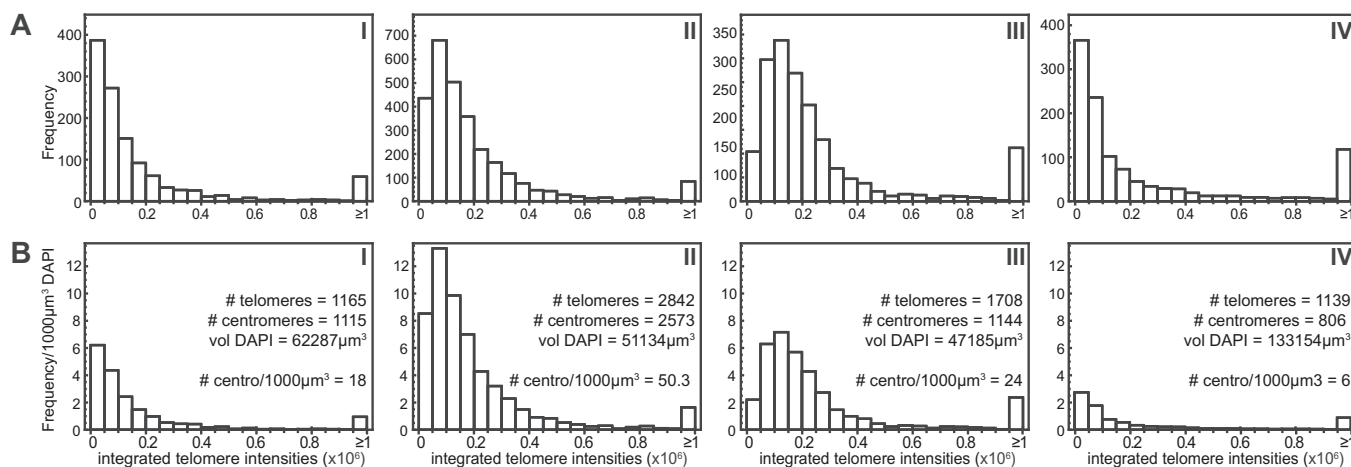


**Fig. 5.** Distribution of telomere signal intensities in different samples of a prostate cancer TMA. Exemplary results from analyses of four samples (I, II, III, IV) from a prostate cancer TMA that was stained using telomeric and centromeric FISH probes. Images were acquired by the 3D-TIM mode, centromere and telomere signals were automatically counted, and telomere signals were analyzed with respect to their integrated intensity. Histograms were generated using 20 bins covering intensity units from 0 to  $1 \times 10^6$  (A. U.). Values  $>1 \times 10^6$  are summarized in the last bin. (A) Distribution of the absolute frequencies of integrated telomere intensities in four different tumor tissue cores from the TMA. (B) Same analysis as in A, only frequencies were normalized to the detected DAPI signal.

tissue regions that should be excluded from the quantitative analysis of the telomere length distribution due to an inefficient FISH reaction. In contrast, regions with normal centromere/DAPI ratio but a low telomere signal can be assigned to cells with very short telomeres. In the future, this analysis can be further improved by reducing the unspecific fluorescent signal that is prominent in the DAPI channel in some of the spots, for example by using different DNA staining reagents and testing agents to reduce autofluorescence, a well-documented issue for FFPE tissues [43]. This will also help to implement a proper automatic segmentation of the nuclei and allow for a cell-based analysis of the FISH signals. Further improvements will include the use of a gradient-flow tracking approach for the cell-based nucleus segmentation as well as an extended artifact detection step that exploits all microscopy channels.

### 3.6. Quantitative confocal microscopy analysis of tissue sections can be used to determine the active TMM

A functional TMM is crucial for unlimited proliferation, a hallmark of tumor cells. Accordingly, several recent studies concluded that the type of active TMM can be exploited for patient

stratification and prognosis [3,4,22–25]. In order to determine the active TMM in primary tumor samples, several characteristic features of ALT can be addressed by different methods depending on the material available. One very reliable marker of ALT activity is the presence of ECTRs that can be visualized by the C-circle assay [17]. This assay, however, requires DNA of high quality isolated from frozen tumor tissues. For FFPE tissues, the detection of APBs by simultaneous PML-IF and FISH hybridization of telomeres is well suited to determine the ALT status (Fig. 2, Fig. 6). FFPE sections from three different pedGBM samples (labeled with I, II, and III) were stained and imaged (Fig. 6A, D). Then an automated 3D image analysis was applied to quantify their telomere length distribution (Fig. 6B, C) as well as the colocalization of telomeres and PML-NBs (Fig. 6C). For this, only specific telomere and PML signals that are localized within the nucleus are considered. Of the three tested pedGBM samples, one tumor (sample III) appears to use the ALT mechanism for telomere maintenance as indicated by a higher frequency of colocalizations between PML protein and telomeres of  $11.0 \pm 4.4\%$  compared to  $4.9 \pm 2.0\%$  and  $4.4 \pm 1.8\%$  (Fig. 6). Thus, the difference between the putatively ALT positive tumor and the other two samples is significant. The error was estimated from independent measurements of tissue slices from an identical

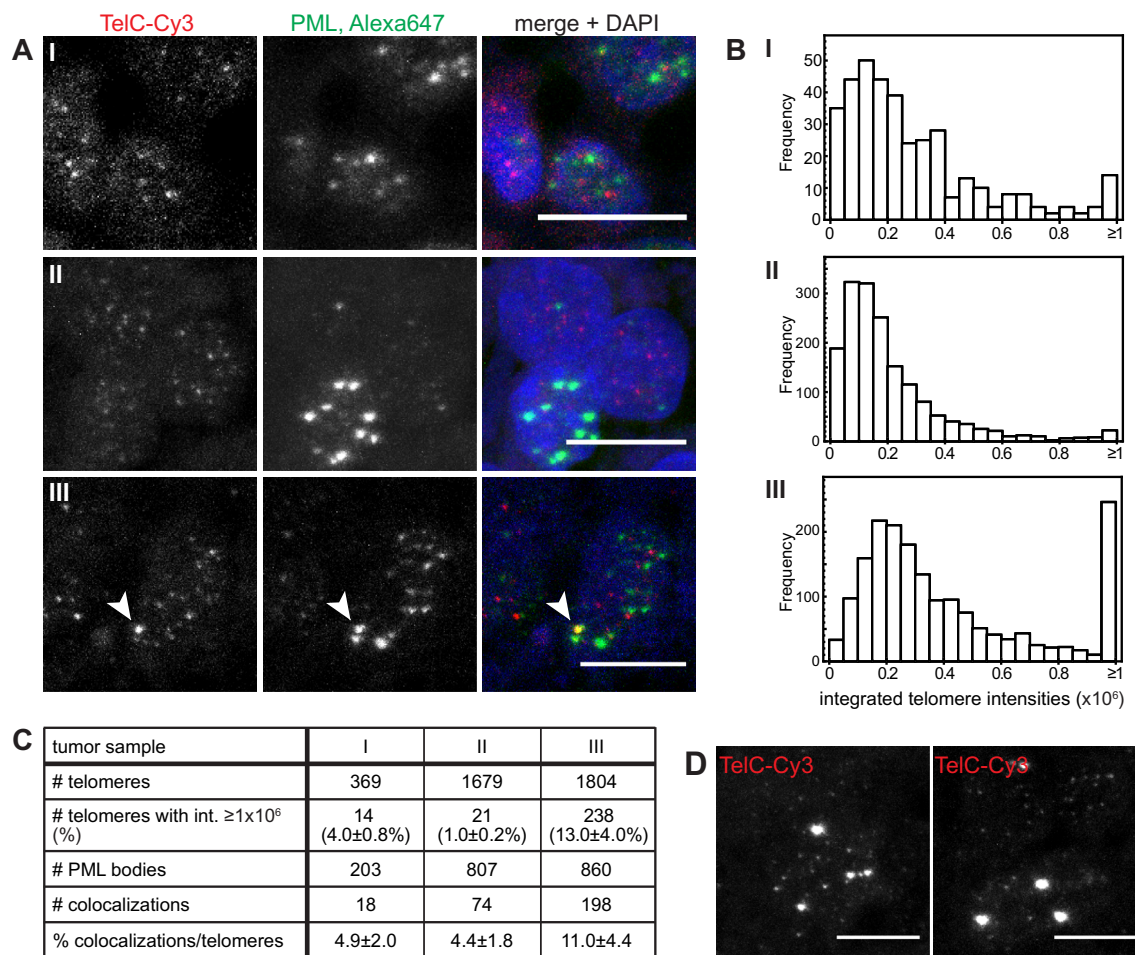


**Fig. 6.** Identification of the ALT status of pedGBM samples from FFPE tissues. (A) Representative CLSM images from tissue sections of three pedGBM samples (I, II, III) stained for telomeres and PML protein. A colocalizing telomere and PML signal in tissue section III is indicated by an arrow. (B) The distributions of telomere lengths in the analyzed tumors are visualized as histograms of the integrated telomere intensities as determined from the respective tissue sections by automated 3D image analysis of the CLSM images. Note the high number of telomeres with an integrated intensity of  $\geq 1 \times 10^6$  (A.U.) in the APB containing tumor III compared to the other tumor samples that do not show ALT specific features (see also Fig. 4D). (C) Overview of results from automated image analysis. Telomeres, PML signals, and colocalizations were detected and quantified automatically in the 3D images from the CLSM acquisition as shown in A. Tumor sample III exhibits an increased number of telomeres that colocalize with a PML-NB indicating an active ALT mechanism in this tumor. (D) Examples of cells from tumor section III with very bright telomere spots as detected by the telomere-specific PNA FISH probe. All images are maximum projections. Scale bars, 10  $\mu$ m.

tumor sample. Notably, this APB positive tumor sample also shows a distinct telomere length intensity profile (Fig. 6B, D) with a high portion of more intense telomere signals compared to the APB negative tumors. Indeed,  $13.0 \pm 4.0\%$  of the detected telomere signals exhibited an integrated intensity of  $\geq 1,000,000$  (A.U.) compared with only  $1.0 \pm 0.2\%$  or  $4.0 \pm 0.8\%$  of telomeres with such strong signals in the other two tested tumor samples. ALT positive cells frequently show an elevated telomere repeat content. Most likely this is reflected by the high number of strong signals obtained from the telomere FISH probe in this case (Fig. 6B–D). The detection of these ultra-bright telomeric foci together with the higher number of APBs is evidence for ALT activity in tumor III but not in the other two tumor tissues examined here. Notably, all three samples have ATRX protein expression as shown by immunohistochemistry (Fig. S1). Accordingly, we classify sample III into the class of pediatric glioblastoma ALT cases that do not show a loss of nuclear ATRX despite the otherwise high correlation of ALT and lack of

ATRX in this entity [44]. By extending our data set in the future and combining it with additional assays for ALT we will be able to more precisely define a threshold of APB frequency to classify a tumor as ALT positive. Furthermore, this type of investigation can be extended by the cell-based analysis of a concomitantly applied centromere-specific FISH probe in order to get a more precise understanding of the telomere length distribution of the different samples as explained above.

### 3.7. An integrated super-resolution mode reveals more details on telomeres and PML-NBs in tumor tissue sections

In further analyses, PML-NBs and telomeres in FFPE glioblastoma tissue sections were examined using single molecule localization microscopy (SMLM, Fig. 7 and Section 2.4). In super-resolution techniques based on photoswitching of single fluorescent molecules, only a changing small random subset of

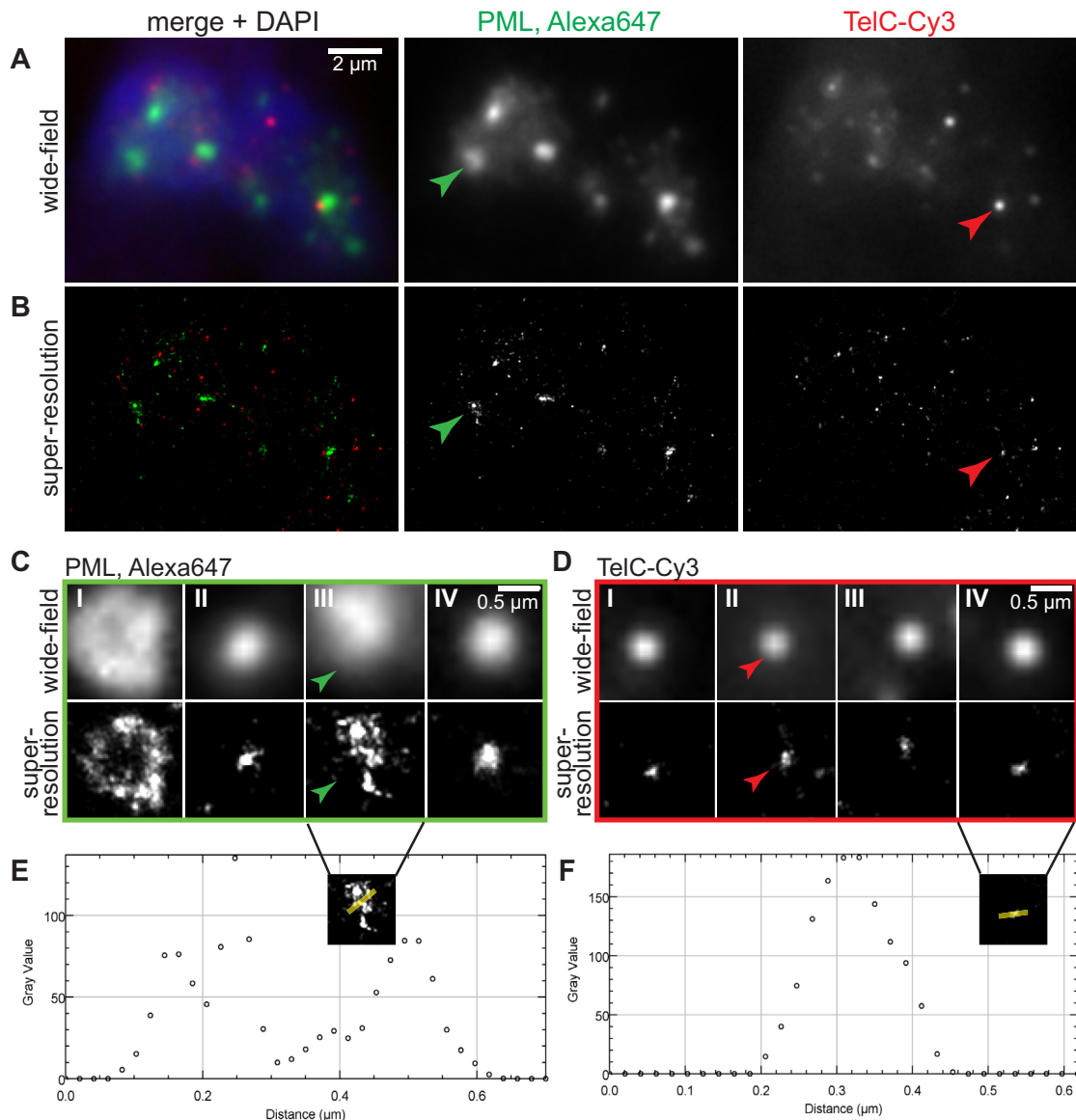


**Fig. 7.** Super-resolution imaging of telomeres and PML-NBs in a pedGBM section. (A) Wide-field overview image of PML-NBs (labeled with Alexa647) and telomeres (labeled with Cy3) in a FFPE pedGBM tissue section. (B) Super-resolution reconstruction of the cell shown in A. (C) Magnified regions of PML-NBs in different cells in the tissue section. In the top row, wide-field images are depicted. In the bottom row, the corresponding super-resolution reconstructions are shown. Green arrows mark a PML-NB identified in panels A and B. (D) Magnified regions of telomeres in different cells in the tissue section (top row: wide-field images, bottom row: super-resolution reconstructions). Red arrows mark a telomere identified in panels A and B. (E) Intensity plot of the PML-NB shown in panel C-III. (F) Intensity plot of the telomere shown in panel D-IV. The plotting direction in E and F is indicated by the yellow line in the insert. (For interpretation of the references to colour in this figure legend, the reader is referred to the web version of this article.)

the fluorophore emits light in a given image frame. Thus, the signals from individual fluorophores can be isolated and fitted by a model function to determine their location with few nanometers accuracy. Usually several thousand image frames are acquired, so that the labeled structures can be reconstructed afterwards based on the fit coordinates [45–49]. Here, laser illumination intensities of about 1 kW/cm<sup>2</sup> were applied without additional variations of the embedding conditions in order to induce photoswitching of the individual fluorophores. With this approach PML-NBs labeled with Alexa647 by immunofluorescence against the PML protein could be resolved in primary tissues and additional information compared to wide-field and CLSM images was inferred (Fig. 7A–C). First, the sizes of the subnuclear structures can be determined in a more precise manner. Here, the measured sizes of the PML-NBs in the super-resolution mode varied from about 100–800 nm. Occasionally, hollow structures with an estimated thickness of the outer shell of about 100 nm were observed (Fig. 7C, I, III). This is in good agreement with previously described characteristics for PML-NBs in U2OS and HeLa cell lines detected with 4Pi super-resolution microscopy [12]. In accordance with previous reports on the structure of these nuclear bodies in cell lines, we could detect an irregular distribution of PML protein on the outer shell in the primary tumor tissue sections [12]. Besides the larger structures, several smaller spots of enriched PML signal were also detected (Fig. 7C, II and IV). They might represent stress-induced PML microbodies or nuclear microspeckled structures as have been described before [50], but this needs further confirmation. Notably, the Cy3 dye, which previously has been reported to undergo photoswitching but produce only low quality reconstruction images [51], could also be used for the localization approach in the tissue sections (Fig. 7B, D). Using the super-resolution mode on the Cy3-labeled telomeres we were able to detect an increased number of telomere signals (Fig. 7A, B). On the other hand, telomere and PML signals can appear as colocalizing when images are acquired in wide-field mode, but upon visualization with higher resolution separated signals can be revealed. Thus, super-resolution microscopy is likely to provide more accurate APB numbers. This underlines the importance of the resolution that is used to acquire images from tissues and that this should be noted when comparing frequencies of colocalizations from different studies. Further, the sizes of telomere signals can be assessed more precisely using super-resolving methods for short telomeres (Fig. 7D, F) than with confocal microscopy when the extension of the telomeric signal is at the border or even below the resolution limit. In the future this could be exploited for a more accurate determination of the telomere length distribution. With simultaneous use of Alexa647-labeled PML protein and the Cy3-labeled telomere FISH probe, coordinate based analyses of the single molecule distributions become feasible [52–54]. Thus, this approach can also be applied to get further insight into the structure of APBs in ALT positive tumor tissues and to compare these findings to previous studies on APBs in cell culture models.

#### 4. Concluding remarks

The identification of telomere features in primary tumor tissue sections is becoming increasingly relevant for patient stratification in several cancer types. Here, we have introduced an integrated workflow for automated 3D high-resolution image acquisition and analysis to dissect telomere features from tissue sections. Using these methods telomere length distribution patterns in single pedGBM tissue sections as well as on a prostate cancer TMA could be determined. We show that the automated acquisition and image analysis of FISH stained TMAs can be used to discriminate telomere length distributions in different patient samples. It is noted that telomere shortening in both prostate cancer cells and

surrounding stromal cells have been suggested as prognostic markers in this disease that is associated with tumorigenesis [32,55–57]. It was found that short or heterogeneous telomere lengths in tumor cells and short telomeres in cancer-associated stromal cells are correlated with a poorer prognosis and higher risk of cancer recurrence. Further, the simultaneous detection of PML protein and telomeres and the workflow proposed here enables the quantitative evaluation of APBs. These nuclear subcompartments are a hallmark for ALT positive tumor cells, and thus provide information about the active TMM. This is of particular interest for pedGBMs where recent studies indicate that the activation of ALT is linked to differences in clinical outcome and therapy response [25]. Thus, the correlation of the 3D-TIM based analysis of telomere features of tissue sections with clinical data can provide an additional readout that can be integrated into patient stratification schemes. To further advance this application additional steps can be implemented in the future, for example an additional tissue-specific staining to discern tumor and normal cells. Super-resolution microscopy techniques are currently hardly exploited for the analysis of cancer tissue sections and provide new possibilities to investigate cellular substructures with respect to cancer-specific aberrations. With the fluorescent labeling scheme used here, a multi-mode and multi-scale imaging approach that combines wide-field microscopy, CLSM, and SMLM within a single instrument can be applied to primary tumor samples. By switching back and forth between the three different imaging modalities, imaging speed and resolution can be optimized for acquiring the specific datasets needed. We anticipate that this approach will also be useful to investigate the structural organization of healthy cells within their endogenous tissue environment.

#### Author contributions

IC and KR designed the study. MG, IC and KID acquired experimental data with the imaging routines developed by MG. SW developed and applied the 3D image analysis approach and performed the statistical analysis of the results. RS, GS, DTWJ and AK coordinated sample acquisition and provided materials. MG, IC and KR analyzed and interpreted the data with contributions from all authors. Experimental design, 3D image analysis, data analysis, and execution were overseen by KaRo, HE and KR. Manuscript writing was done by IC, MG, SW and KR with contributions from all authors regarding critical revisions.

#### Acknowledgments

We thank David Capper (Department of Neuropathology, Heidelberg University Hospital) for performing IHC stainings. The work was funded by the German Federal Ministry of Education and Research (BMBF) within project CancerTelSys (grant number 01ZX1302) in the e:Med program. The ViroQuant-CellNetworks RNAi Screening Facility was supported by project HD-HuB (grant number 031A537C) in the BMBF de.NBI program and by the CellNetworks-Cluster of Excellence (grant number EXC81).

#### Appendix A. Supplementary data

Supplementary data associated with this article can be found, in the online version, at <http://dx.doi.org/10.1016/j.ymeth.2016.09.014>.

#### References

- [1] W. Palm, T. de Lange, How shelterin protects mammalian telomeres, *Annu. Rev. Genet.* 42 (2008) 301–334.
- [2] B. Heidenreich, P.S. Rachakonda, K. Hemminki, R. Kumar, TERT promoter mutations in cancer development, *Curr. Opin. Genet. Dev.* 24 (2014) 30–37.

- [3] M. Peifer, F. Hertwig, F. Roels, D. Dredix, M. Gartlgruber, R. Menon, A. Kramer, J.L. Roncaioli, F. Sand, J.M. Heuckmann, F. Ikram, R. Schmidt, S. Ackermann, A. Engesser, Y. Kahlert, W. Vogel, J. Altmüller, P. Nürnberg, J. Thierry-Mieg, D. Thierry-Mieg, A. Mariappan, S. Heynck, E. Mariotti, K.O. Henrich, C. Gloeckner, G. Bosco, I. Leuschner, M.R. Schweiger, L. Savellyeva, S.C. Watkins, C. Shao, E. Bell, T. Hofer, V. Achter, U. Lang, J. Theissen, R. Volland, M. Saadati, A. Eggert, B. de Wilde, F. Berthold, Z. Peng, C. Zhao, L. Shi, M. Ortmann, R. Buttner, S. Perner, B. Hero, A. Schramm, J.H. Schulte, C. Herrmann, R.J. O'Sullivan, F. Westermann, R.K. Thomas, M. Fischer, Telomerase activation by genomic rearrangements in high-risk neuroblastoma, *Nature* 526 (7575) (2015) 700–704.
- [4] L.J. Valentijn, J. Koster, D.A. Zwijnenburg, N.E. Hasselt, P. van Sluis, R. Volckmann, M.M. van Noesel, R.E. George, G.A. Tytgat, J.J. Molenaar, R. Versteeg, TERT rearrangements are frequent in neuroblastoma and identify aggressive tumors, *Nat. Genet.* (2015).
- [5] C.M. Heaphy, R.F. de Wilde, Y. Jiao, A.P. Klein, B.H. Edil, C. Shi, C. Bettogowda, F. J. Rodriguez, C.G. Eberhart, S. Hebbard, G.J. Offerhaus, R. McLendon, B.A. Rasheed, Y. He, H. Yan, D.D. Bigner, S.M. Oba-Shinjo, S.K. Marie, G.J. Riggins, K. W. Kinzler, B. Vogelstein, R.H. Hruban, A. Maitra, N. Papadopoulos, A.K. Meeker, Altered telomeres in tumors with ATRX and DAXX mutations, *Science* 333 (6041) (2011) 425.
- [6] J.D. Henson, R.R. Reddel, Assaying and investigating alternative lengthening of telomeres activity in human cells and cancers, *FEBS Lett.* 584 (17) (2010) 3800–3811.
- [7] R.L. Dilley, R.A. Greenberg, Alternative telomere maintenance and cancer, *Trends Cancer* 1 (2) (2015) 145–156.
- [8] T.M. Bryan, A. Englezou, J. Gupta, S. Bacchetti, R.R. Reddel, Telomere elongation in immortal human cells without detectable telomerase activity, *EMBO J.* 14 (17) (1995) 4240–4248.
- [9] I. Chung, S. Osterwald, K.I. Deeg, K. Rippe, PML body meets telomere: the beginning of an ALTernate ending?, *Nucleus* 3 (3) (2012) 263–275.
- [10] I. Chung, H. Leonhardt, K. Rippe, De novo assembly of a PML nuclear subcompartment occurs through multiple pathways and induces telomere elongation, *J. Cell Sci.* 124 (Pt 21) (2011) 3603–3618.
- [11] T.R. Yeager, A.A. Neumann, A. Englezou, L.I. Huschtscha, J.R. Noble, R.R. Reddel, Telomerase-negative immortalized human cells contain a novel type of promyelocytic leukemia (PML) body, *Cancer Res.* 59 (17) (1999) 4175–4179.
- [12] M. Lang, T. Jegou, I. Chung, K. Richter, S. Munch, A. Udvarhelyi, C. Cremer, P. Hemmerich, J. Engelhardt, S.W. Hell, K. Rippe, Three-dimensional organization of promyelocytic leukemia nuclear bodies, *J. Cell Sci.* 123 (Pt 3) (2010) 392–400.
- [13] C.A. Lovejoy, W. Li, S. Reisenweber, S. Thongthip, J. Bruno, T. de Lange, S. De, J. H. Petrini, P.A. Sung, M. Jasin, J. Rosenbluh, Y. Zwang, B.A. Weir, C. Hatton, E. Ivanova, L. Macconail, M. Hanna, W.C. Hahn, N.F. Lue, R.R. Reddel, Y. Jiao, K. Kinzler, B. Vogelstein, N. Papadopoulos, A.K. Meeker, A.L.T.S.C. Consortium, Loss of ATRX, genome instability, and an altered DNA damage response are hallmarks of the alternative lengthening of telomeres pathway, *PLoS Genet.* 8 (7) (2012) e1002772.
- [14] D. Sturm, H. Witt, V. Hovestadt, D.A. Khuong-Quang, D.T. Jones, C. Konermann, E. Pfaff, M. Tonjes, M. Sill, S. Bender, M. Kool, M. Zapatka, N. Becker, M. Zucknick, T. Hielscher, X.Y. Liu, A.M. Fontebasso, M. Ryzhova, S. Albrecht, K. Jacob, M. Wolter, M. Ebinger, M.U. Schuhmann, T. van Meter, M.C. Fruhwald, H. Hauch, A. Pekrun, B. Radlwimmer, T. Niehues, G. von Kumorowski, M. Durken, A.E. Kulozik, J. Madden, A. Donson, N.K. Foreman, R. Drissi, M. Fouladi, W. Scheurlen, A. von Deimling, C. Monoranu, W. Roggendorf, C. Herold-Mende, A. Unterberg, C.M. Kramm, J. Felsberg, C. Hartmann, B. Wiestler, W. Wick, T. Milde, O. Witt, A.M. Lindroth, J. Schwartzentruber, D. Faury, A. Fleming, M. Zakrzewska, P.P. Liberski, K. Zakrzewski, P. Hauser, M. Garami, A. Klekner, L. Bognar, S. Morrissy, F. Cavalli, M.D. Taylor, P. van Sluis, J. Koster, R. Versteeg, R. Volckmann, T. Mikkelsen, K. Aldape, G. Reifenberger, V.P. Collins, J. Majewski, A. Korshunov, P. Lichter, C. Plass, N. Jabado, S.M. Pfister, Hotspot mutations in H3F3A and IDH1 define distinct epigenetic and biological subgroups of glioblastoma, *Cancer Cell* 22 (4) (2012) 425–437.
- [15] J. Schwartzentruber, A. Korshunov, X.Y. Liu, D.T. Jones, E. Pfaff, K. Jacob, D. Sturm, A.M. Fontebasso, D.A. Quang, M. Tonjes, V. Hovestadt, S. Albrecht, M. Kool, A. Nantel, C. Konermann, A. Lindroth, N. Jager, T. Rausch, M. Ryzhova, J.O. Korbel, T. Hielscher, P. Hauser, M. Garami, A. Klekner, L. Bognar, M. Ebinger, M. U. Schuhmann, W. Scheurlen, A. Pekrun, M.C. Fruhwald, W. Roggendorf, C. Kramm, M. Durken, J. Atkinson, P. Lepage, A. Montpetit, M. Zakrzewska, K. Zakrzewski, P.P. Liberski, Z. Dong, P. Siegel, A.E. Kulozik, M. Zapatka, A. Guha, D. Malkin, J. Felsberg, G. Reifenberger, A. von Deimling, K. Ichimura, V.P. Collins, H. Witt, T. Milde, O. Witt, C. Zhang, P. Castelo-Branco, P. Lichter, D. Faury, U. Tabori, C. Plass, J. Majewski, S.M. Pfister, N. Jabado, Driver mutations in histone H3.3 and chromatin remodelling genes in paediatric glioblastoma, *Nature* 482 (7384) (2012) 226–231.
- [16] A.J. Cesare, J.D. Griffith, Telomeric DNA in ALT cells is characterized by free telomeric circles and heterogeneous t-loops, *Mol. Cell Biol.* 24 (22) (2004) 9948–9957.
- [17] J.D. Henson, Y. Cao, L.I. Huschtscha, A.C. Chang, A.Y. Au, H.A. Pickett, R.R. Reddel, DNA C-circles are specific and quantifiable markers of alternative-lengthening-of-telomeres activity, *Nat. Biotechnol.* 27 (12) (2009) 1181–1185.
- [18] D. Conomos, M.D. Stutz, M. Hills, A.A. Neumann, T.M. Bryan, R.R. Reddel, H.A. Pickett, Variant repeats are interspersed throughout the telomeres and recruit nuclear receptors in ALT cells, *J. Cell Biol.* 199 (6) (2012) 893–906.
- [19] H.A. Pickett, R.R. Reddel, Molecular mechanisms of activity and derepression of alternative lengthening of telomeres, *Nat. Struct. Mol. Biol.* 22 (11) (2015) 875–880.
- [20] K. Rippe, B. Luke, TERRA and the state of the telomere, *Nat. Struct. Mol. Biol.* 22 (11) (2015) 853–858.
- [21] C.M. Azzalin, P. Reichenbach, L. Khoriauli, E. Giulotto, J. Lingner, Telomeric repeat containing RNA and RNA surveillance factors at mammalian chromosome ends, *Science* 318 (5851) (2007) 798–801.
- [22] K.L. McDonald, J. McDonnell, A. Muntoni, J.D. Henson, M.E. Hegi, A. von Deimling, H.R. Wheeler, R.J. Cook, M.T. Biggs, N.S. Little, B.G. Robinson, R.R. Reddel, J.A. Royds, Presence of alternative lengthening of telomeres mechanism in patients with glioblastoma identifies a less aggressive tumor type with longer survival, *J. NeuroPathol. Exp. Neurol.* 69 (7) (2010) 729–736.
- [23] E. Dogeas, G. Karagkounis, C.M. Heaphy, K. Hirose, T.M. Pawlik, C.L. Wolfgang, A. Meeker, R.H. Hruban, J.L. Cameron, M.A. Choti, Alternative lengthening of telomeres predicts site of origin in neuroendocrine tumor liver metastases, *J. Am. Coll. Surg.* 218 (4) (2014) 628–635.
- [24] V. Hakin-Smith, D.A. Jellinek, D. Levy, T. Carroll, M. Teo, W.R. Timperley, M.J. McKay, R.R. Reddel, J.A. Royds, Alternative lengthening of telomeres and survival in patients with glioblastoma multiforme, *Lancet* 361 (9360) (2003) 836–838.
- [25] D. Sturm, S. Bender, D.T. Jones, P. Lichter, J. Grill, O. Becher, C. Hawkins, J. Majewski, C. Jones, J.F. Costello, A. Iavarone, K. Aldape, C.W. Brennan, N. Jabado, S.M. Pfister, Paediatric and adult glioblastoma: multifactorial (epi) genomic culprits emerge, *Nat. Rev. Cancer* 14 (2) (2014) 92–107.
- [26] A.K. Meeker, W.R. Gage, J.L. Hicks, I. Simon, J.R. Coffman, E.A. Platz, G.E. March, A.M. De Marzo, Telomere length assessment in human archival tissues: combined telomere fluorescence in situ hybridization and immunostaining, *Am. J. Pathol.* 160 (4) (2002) 1259–1268.
- [27] C.M. Heaphy, A.K. Meeker, The potential utility of telomere-related markers for cancer diagnosis, *J. Cell Mol. Med.* 15 (6) (2011) 1227–1238.
- [28] A.J. Cesare, C.M. Heaphy, R.J. O'Sullivan, Visualization of telomere integrity and function in vitro and in vivo using immunofluorescence techniques, *Curr. Protoc. Cytom.* 73 (2015), 12.40.1–40.
- [29] C.M. Heaphy, A.P. Subhawong, S.M. Hong, M.G. Goggins, E.A. Montgomery, E. Gabrielson, G.J. Netto, J.I. Epstein, T.L. Lotan, W.H. Westra, M. Shih, C.A. Iacobuzio-Donahue, A. Maitra, Q.K. Li, C.G. Eberhart, J.M. Taube, D. Rakheja, R.J. Kurman, T.C. Wu, R.B. Roden, P. Argani, A.M. De Marzo, L. Terracciano, M. Torbenson, A.K. Meeker, Prevalence of the alternative lengthening of telomeres telomere maintenance mechanism in human cancer subtypes, *Am. J. Pathol.* 179 (4) (2011) 1608–1615.
- [30] A. Pezzolo, A. Pistorio, C. Gambini, R. Haupt, M. Ferraro, G. Erminio, B. De Bernardi, A. Garaventa, V. Pistoia, Intratumoral diversity of telomere length in individual neuroblastoma tumors, *Oncotarget* 6 (10) (2015) 7493–7503.
- [31] X. Zhou, A.K. Meeker, K.H. Makambi, O. Kosti, B.V. Kallakury, M.K. Sidawy, C.A. Loffredo, Y.L. Zheng, Telomere length variation in normal epithelial cells adjacent to tumor: potential biomarker for breast cancer local recurrence, *Carcinogenesis* 33 (1) (2012) 113–118.
- [32] C.M. Heaphy, G.S. Yoon, S.B. Pesko, C.E. Joshi, T.K. Lee, E. Giovannucci, L.A. Mucci, S.A. Kenfield, M.J. Stampfer, J.L. Hicks, A.M. De Marzo, E.A. Platz, A.K. Meeker, Prostate cancer cell telomere length variability and stromal cell telomere length as prognostic markers for metastasis and death, *Cancer Discov.* 3 (10) (2013) 1130–1141.
- [33] A.M. Joshua, B. Vukovic, I. Braude, S. Hussein, M. Zielenska, J. Srigley, A. Evans, J.A. Squire, Telomere attrition in isolated high-grade prostatic intraepithelial neoplasia and surrounding stroma is predictive of prostate cancer, *Neoplasia* 9 (1) (2007) 81–89.
- [34] S. Osterwald, K.I. Deeg, I. Chung, D. Parisotto, S. Wörz, K. Rohr, H. Erfle, K. Rippe, PML induces compaction, TRF2 depletion and DNA damage signaling at telomeres and promotes their alternative lengthening, *J. Cell Sci.* 128 (10) (2015) 1887–1900.
- [35] S. Osterwald, S. Wörz, J. Reymann, F. Sieckmann, K. Rohr, H. Erfle, K. Rippe, A three-dimensional colocalization RNA interference screening platform to elucidate the alternative lengthening of telomeres pathway, *Biotechnol. J.* 7 (1) (2012) 103–116.
- [36] J. Kononen, L. Bubendorf, A. Kallioniemi, M. Barlund, P. Schraml, S. Leighton, J. Torhorst, M.J. Mihatsch, G. Sauter, O.P. Kallioniemi, Tissue microarrays for high-throughput molecular profiling of tumor specimens, *Nat. Med.* 4 (7) (1998) 844–847.
- [37] M. Ovesny, P. Krizek, J. Borkovec, Z. Svindrych, G.M. Hagen, ThunderSTORM: a comprehensive ImageJ plug-in for PALM and STORM data analysis and super-resolution imaging, *Bioinformatics* 30 (16) (2014) 2389–2390.
- [38] S. Wörz, P. Sander, M. Pfannmüller, R.J. Rieker, S. Joos, G. Mechttersheimer, P. Boukamp, P. Lichter, K. Rohr, 3D Geometry-based quantification of colocalizations in multi-channel 3D microscopy images of human soft tissue tumors, *IEEE Trans. Medical Imaging* 29 (2010) 1474–1484.
- [39] S. Eck, S. Wörz, K. Müller-Ott, M. Hahn, A. Biesdorf, G. Schotta, K. Rippe, K. Rohr, A spherical harmonics intensity model for 3D segmentation and 3D shape analysis of heterochromatin foci, *Med. Image Anal.* 32 (2016) 18–31.
- [40] M.A. Cerone, C. Autexier, J.A. Londoño-Vallejo, S. Bacchetti, A human cell line that maintains telomeres in the absence of telomerase and of key markers of ALT, *Oncogene* 24 (53) (2005) 7893–7901.
- [41] C.L. Fasching, K. Bower, R.R. Reddel, Telomerase-independent telomere length maintenance in the absence of alternative lengthening of telomeres-associated promyelocytic leukemia bodies, *Cancer Res.* 65 (7) (2005) 2722–2729.
- [42] R.A. Marciniak, D. Cavazos, R. Montellano, Q. Chen, L. Guarente, F.B. Johnson, A novel telomere structure in a human alternative lengthening of telomeres cell line, *Cancer Res.* 65 (7) (2005) 2730–2737.

- [43] M.S. Viegas, T.C. Martins, F. Seco, A. do Carmo, An improved and cost-effective methodology for the reduction of autofluorescence in direct immunofluorescence studies on formalin-fixed paraffin-embedded tissues, *Eur. J. Histochem.* 51 (1) (2007) 59–66.
- [44] M. Abedalthagafi, J.J. Phillips, G.E. Kim, S. Mueller, D.A. Haas-Kogen, R.E. Marshall, S.E. Croul, M.R. Santi, J. Cheng, S. Zhou, L.M. Sullivan, M. Martinez-Lage, A.R. Judkins, A. Perry, The alternative lengthening of telomere phenotype is significantly associated with loss of ATRX expression in high-grade pediatric and adult astrocytomas: a multi-institutional study of 214 astrocytomas, *Mod. Pathol.* 26 (11) (2013) 1425–1432.
- [45] E. Betzig, G.H. Patterson, R. Sougrat, O.W. Lindwasser, S. Olenych, J.S. Bonifacino, M.W. Davidson, J. Lippincott-Schwartz, H.F. Hess, Imaging intracellular fluorescent proteins at nanometer resolution, *Science* 313 (5793) (2006) 1642–1645.
- [46] P. Lemmer, M. Gunkel, D. Baddeley, R. Kaufmann, A. Urich, Y. Weiland, J. Reymann, P. Müller, M. Hausmann, C. Cremer, SPDM: light microscopy with single-molecule resolution at the nanoscale, *Appl. Phys. B* 93 (2008) 1–12.
- [47] M. Heilemann, S. van de Linde, M. Schüttelpe, R. Kasper, B. Seefeldt, A. Mukherjee, P. Tinnefeld, M. Sauer, Subdiffraction-resolution fluorescence imaging with conventional fluorescent probes, *Angew. Chem. Int. Ed. Engl.* 47 (33) (2008) 6172–6176.
- [48] J. Fölling, M. Bossi, H. Bock, R. Medda, C.A. Wurm, B. Hein, S. Jakobs, C. Eggeling, S.W. Hell, Fluorescence nanoscopy by ground-state depletion and single-molecule return, *Nat. Methods* 5 (11) (2008) 943–945.
- [49] M.J. Rust, M. Bates, X. Zhuang, Sub-diffraction-limit imaging by stochastic optical reconstruction microscopy (STORM), *Nat. Methods* 3 (2006) 793–796.
- [50] V. Lallemand-Breitenbach, H. de The, PML nuclear bodies, *Cold Spring Harb. Perspect. Biol.* 2 (5) (2010) a000661.
- [51] G.T. Dempsey, J.C. Vaughan, K.H. Chen, M. Bates, X. Zhuang, Evaluation of fluorophores for optimal performance in localization-based super-resolution imaging, *Nat. Methods* 8 (12) (2011) 1027–1036.
- [52] M. Gunkel, F. Erdel, K. Rippe, P. Lemmer, R. Kaufmann, C. Hormann, R. Amberger, C. Cremer, Dual color localization microscopy of cellular nanostructures, *Biotechnol. J.* 4 (6) (2009) 927–938.
- [53] S. Malkusch, U. Endesfelder, J. Mondry, M. Gelleri, P.J. Verwee, M. Heilemann, Coordinate-based colocalization analysis of single-molecule localization microscopy data, *Histochem. Cell Biol.* 137 (1) (2012) 1–10.
- [54] B. Flottmann, M. Gunkel, T. Lisauskas, M. Heilemann, V. Starkuviene, J. Reymann, H. Erfle, Correlative light microscopy for high-content screening, *Biotechniques* 55 (5) (2013) 243–252.
- [55] A.K. Meeker, J.L. Hicks, E.A. Platz, G.E. March, C.J. Bennett, M.J. Delannoy, A.M. De Marzo, Telomere shortening is an early somatic DNA alteration in human prostate tumorigenesis, *Cancer Res.* 62 (22) (2002) 6405–6409.
- [56] C.A. Fordyce, C.M. Heaphy, N.E. Joste, A.Y. Smith, W.C. Hunt, J.K. Griffith, Association between cancer-free survival and telomere DNA content in prostate tumors, *J. Urol.* 173 (2) (2005) 610–614.
- [57] C.M. Heaphy, G. Gaonkar, S.B. Peskoe, C.E. Joshi, A.M. De Marzo, M.S. Lucia, P.J. Goodman, S.M. Lippman, I.M. Thompson Jr., E.A. Platz, A.K. Meeker, Prostate stromal cell telomere shortening is associated with risk of prostate cancer in the placebo arm of the Prostate Cancer Prevention Trial, *Prostate* 75 (11) (2015) 1160–1166.

## **Supplementary Information**

### **Quantification of telomere features in tumor tissue sections by an automated 3D imaging-based workflow**

Manuel Gunkel, Inn Chung, Stefan Wörz, Katharina I. Deeg, Ronald Simon, Guido Sauter, David T.W. Jones, Andrey Korshunov, Karl Rohr, Holger Erfle and Karsten Rippe

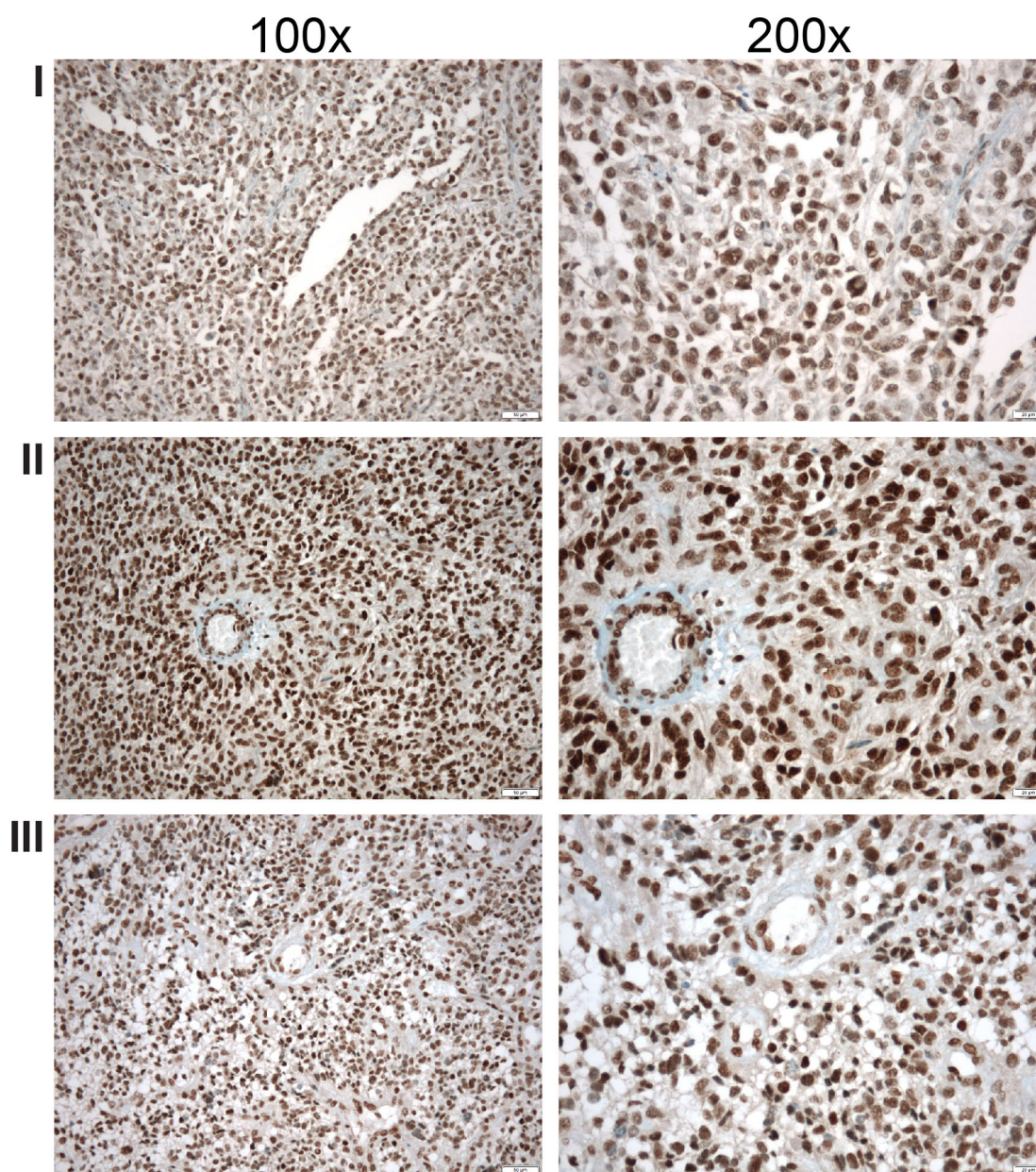
#### **Supplementary Information includes:**

Supplementary Figure S1, ATRX immunohistochemical staining of pedGBM tissues

Supplementary Protocol 1, Targeted imaging workflow implementation in KNIME

Supplementary Protocol 2, 3D model-based image analysis quantification of subcellular structures

KNIME workflows "identifyCells" and "referencingTMA" provided as supplementary files for download

**Supplementary Figure S1**

**Fig. S1.** ATRX immunohistochemical staining of pedGBM tumors. The same three pedGBM tumors analyzed in Fig. 6 were evaluated for the presence of ATRX protein by immunohistochemistry. ATRX expression was detected in all three tumor tissues. 100x and 200x magnifications are shown.



## Supplementary Protocol 1

### Targeted imaging workflow implementation in KNIME

#### 1. Image acquisition for ROI coordinate assignment

To perform a coordinate transfer between two microscope systems and to locate preselected ROIs after repositioning a sample it is mandatory to assign a set of matching coordinates on both systems. In the case of imaging the TMAs as described in the main text, the whole sample was already imaged on the wide-field microscope. To obtain a matching pair of coordinates, the sample was placed on the stage of the confocal Leica SP5.

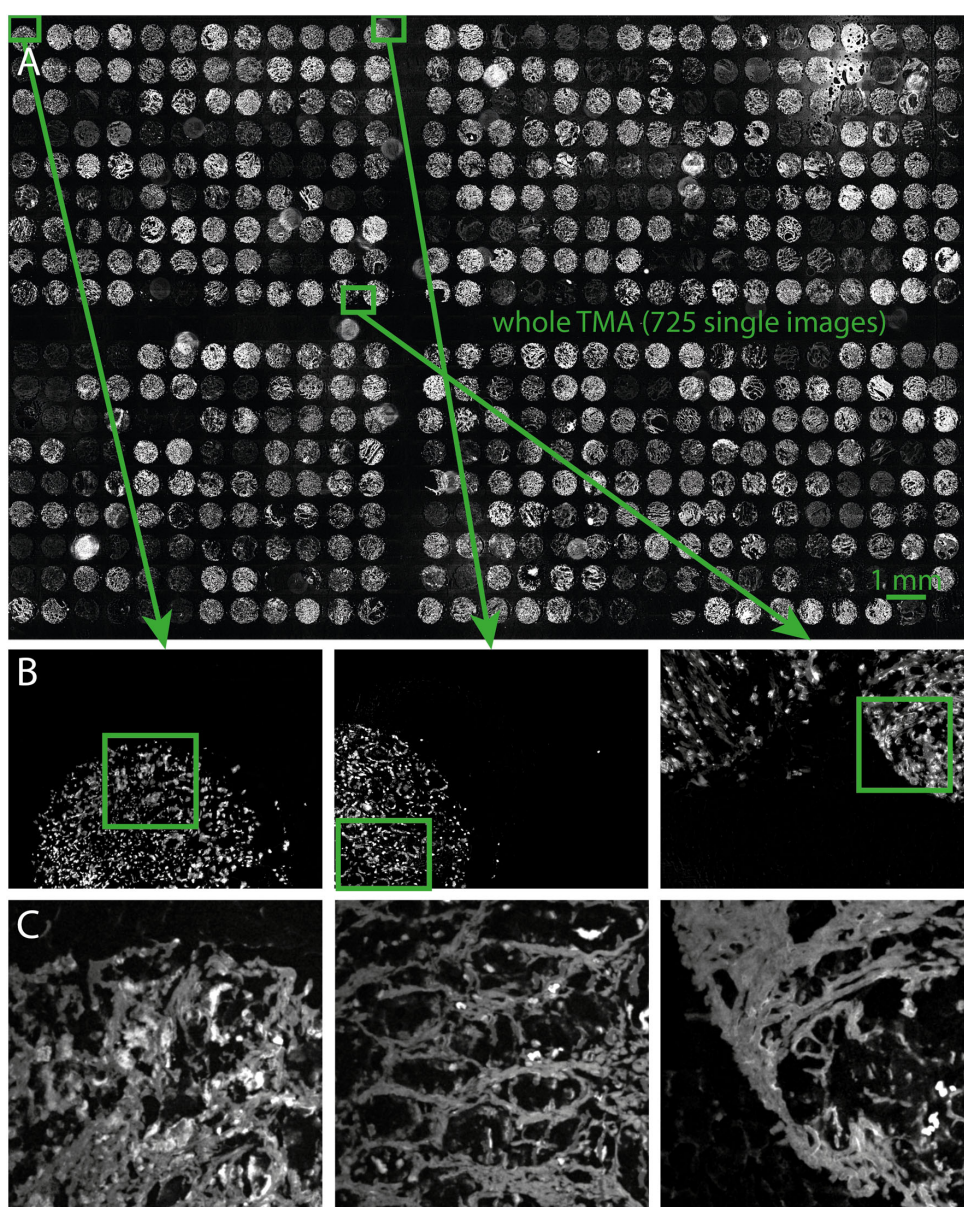


**Fig. S2.** Coordinate assignment scheme for referencing. (A) A complete TMA is imaged by wide-field microscopy. (B) Images are also acquired with a confocal microscope at selected positions indicated by the green rectangles. (C) Enlarged view of the reference confocal image regions that are matched to the wide-field images.

The sample was positioned so that the top left core was visible in the field of view of the microscope and this position added to the 'Mark-and-Find' section within the Leica LAS-AF software. This was repeated for 11 cores to the right and for 8 cores down (Fig. S2A). This sequence is arbitrary but a sufficient distance between the single reference position results in higher accuracy of the referencing process. The position list was saved in a \*.maf file and the imaging sequence started, which acquired one reference image at each position (Fig. S2C). These images were stored in a \*.lif container and are matched together with the position information from the \*.maf-file to the wide-field data set as described for the 'referencingTMA' workflow below.

## 2. Installing and configuring KNIME

The automated targeted image acquisition is implemented with the KNIME open source data analysis platform. KNIME allows it to visually create a data processing pipeline that executes the analysis steps and evaluates the results and images. These pipelines are referred to as 'KNIME workflows'. In this manner images are acquired from regions that contain the biologically relevant information, which largely speeds up the imaging process. KNIME can be installed from [www.knime.org](http://www.knime.org) and additional plugins needed are loaded from the following repositories:

<http://update.knime.org/analytics-platform/3.2>

<http://update.knime.org/community-contributions/trusted/3.2>

<http://update.knime.org/community-contributions/3.2>

The targeted imaging KNIME workflows described here can be downloaded as supplementary files termed "identifyCells.zip" and "referencingTMA.zip". Additionally, the plugins listed in Table S1 need to be included since they provide nodes integrated in the workflow. These plugins are added via 'Help' -> 'Install New Software ...'. The workflows themselves are imported by selecting 'File' -> 'Import KNIME Workflow ...'. In the following description of the KNIME workflows, node names are written in *italics*, followed by their short description as stated within the workflows under the nodes in normal type. Metanodes collecting multiple nodes in one single node are marked as such.

Name	Version
KNIME Analytics Platform	3.2.0.v201607131338
KNIME Distance Matrix	3.2.0.v201606131354
KNIME External Tool Support	3.2.0.v201605301230
KNIME File Handling Nodes	3.2.0.v201607061823
KNIME HCS Tools	3.1.101.v201604271109
KNIME Image Processing	1.5.1.201607261306
KNIME Image Processing - ImageJ Integration (Beta)	0.10.1.v201607070911
KNIME JFreeChart	3.2.0.v201605301230
KNIME Public Server Access	3.2.0.v201604201149
KNIME Quick Forms	3.2.0.v201607131237
KNIME Quick Forms (legacy)	3.2.0.v201606131354
KNIME R Statistics Integration (Windows Binaries)	3.0.3.v201607011540
KNIME Virtual Nodes	3.2.0.v201606131354

**Table S1** KNIME analytics platform and plugins used within the workflows presented here.

### 3. KNIME Workflow ‘identifyCells’

The ‘identifyCells’ workflow is depicted in Fig. S3. It retrieves the locations of the images from the prescreen, specifies them (*List Files*: list image locations) and matches them with the corresponding metadata (*File Reader*: read metadata) in order to get the x, y and z position of the microscope (Metanode *calcPositions*). Images are sorted based on their name and processed (Metanode *ImageProcessing*) in a parallel loop structure (*Parallel Chunk Start* and *Parallel Chunk End*). First, the images are retrieved from the specified positions (Image Reader (Table)). Background is subtracted (*ImageJ Macro*: subtract background), and then the images are thresholded globally and locally (*Global Thresholding*, *Local Thresholding*). The resulting binary images are merged (*Binary Image Operations*) and the result is analyzed for connected components (*Connected Component Analysis*). These components are then filtered for size (*Labeling Filter*) and subdivided (*Waehlby Cell Clump Splitter* [1]). For each remaining connected component the following features were extracted (*Image Segment Features*): Mean intensity and its standard deviation, x and y centroid position, number of pixels, circularity, perimeter, convexity, extend, and diameter. The result is a table with one entry for each object listing its features. The name of the original image each object was found in is retrieved (*Labeling Properties*). Post processing (Metanode: *PostProcessing*) is performed in order to keep only objects above a minimum mean intensity. Additionally, the data set is thinned out by a distance filter so that remaining objects have a distance of 25  $\mu\text{m}$  or greater to each other, which resembles one field of view for later targeted imaging. Thus, duplicates of an imaged object are avoided. The table containing the objects and their corresponding information is stored as a KNIME table.

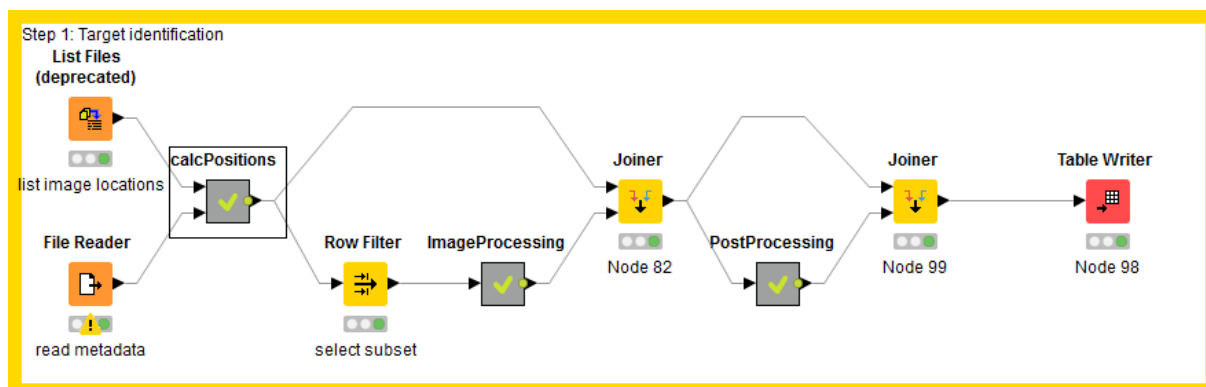
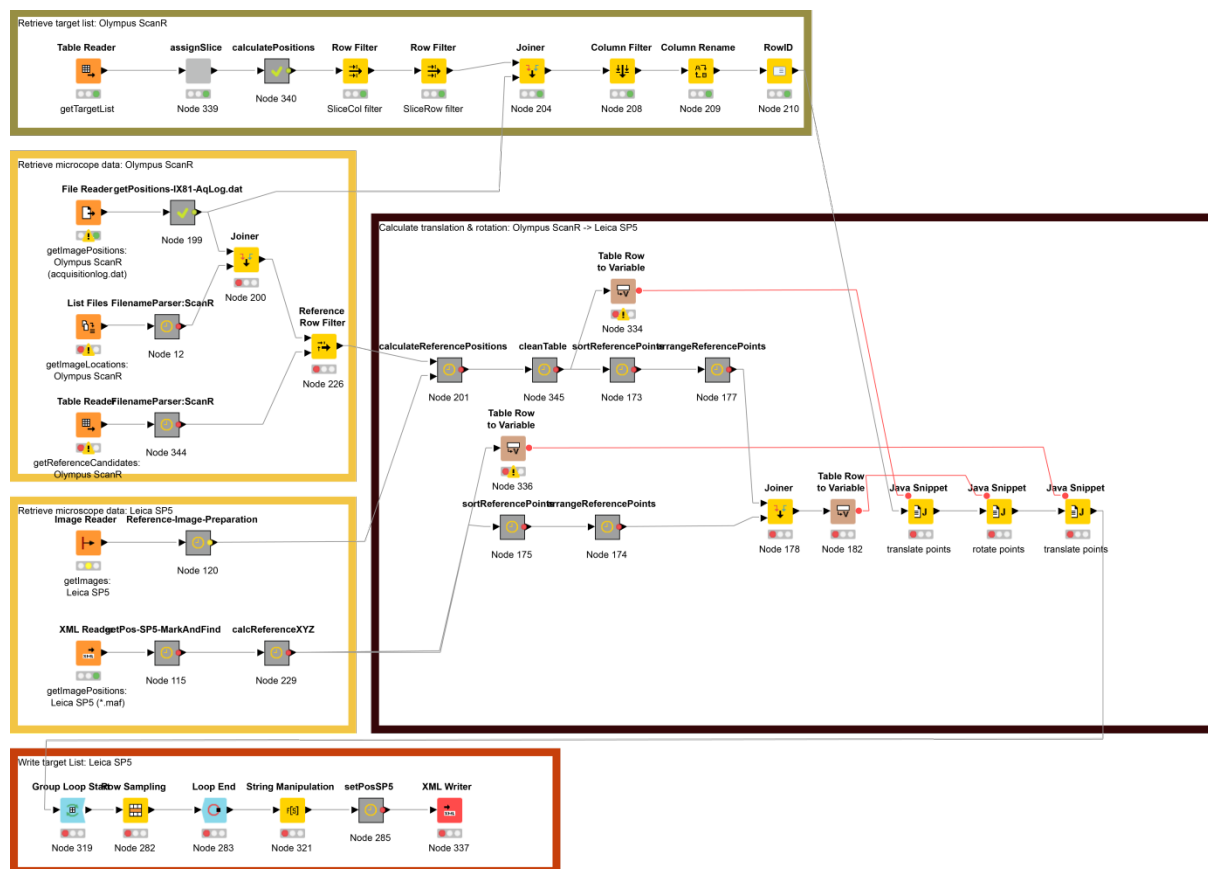


Fig. S3. KNIME workflow ‘identifyCells’

### 4. KNIME Workflow ‘referencingTMA’

The ‘referencingTMA’ workflow consists of 4 steps that are described in further detail below. These comprise (i) obtaining the target list and enriching it with metadata, (ii) retrieving microscope specific data and metadata for the Olympus ScanR and Leica SP5 microscopes, (iii) calculating the coordinate transfer function between the two sets of reference points for each microscope and applying it on the target list, and (iv) generating the target list in a format readable by the microscope (Fig. S4). Position information is stored in  $\mu\text{m}$ .



**Fig. S4.** KNIME workflow ‘referencingTMA’

#### 4.1 Generating the target list and adding metadata

The target list as generated by the workflow ‘identifyCells’ is loaded. Each object of the target list is classified as belonging to one spot on the tissue microarray (Metanode *assign Slice*; double click to configure). Here, the following parameters have to be specified (in  $\mu\text{m}$ ): center positions  $x_0$  and  $y_0$  of the first spot on the TMA (Olympus ScanR coordinates), the row and column distances  $d\text{-row}$  and  $d\text{-col}$  (on the TMA) as well as the Offset  $dx\text{-row}$  and  $dy\text{-row}$  (relative Olympus ScanR coordinates) in case there is an angle between the orientation of the TMA matrix and the microscope coordinate system. In order to find suitable reference candidates within the target list and to account for the heterogeneity observed between the spots, the distribution of the features determined by the workflow ‘identifyCells’ is calculated individually for each spot and filters are adapted to these levels (Metanode *calculatePositions*). For each object, the according microscope specific metadata is assigned (*Joiner*) and the table is cleaned (*Column Filter*, *Column Rename*, *RowID*).

#### 4.2 Retrieving microscope specific data and metadata

The microscope systems used here were an Olympus ScanR and Leica SP5. For the Olympus ScanR, the locations of the acquired images (*List Files*: *getImageLocations*: Olympus ScanR) as well as the microscope specific metadata (*File Reader*: *getImagePositions*: Olympus ScanR (acquisitionlog.dat)) are read in, parsed (Metanodes

*getPositionsIX81-AqLog.dat* and *FilenameParser:ScanR*) and joined in a single table (*Joiner*). For referencing, images are compared between the two microscope systems. It is possible to search the acquired reference images of system 2 in the complete data set of system 1. Here it is beneficial that we know beforehand in which core sections on the TMA reference images were acquired. The names of all the corresponding images in the data set of system 1 are provided within a KNIME table (*Table Reader: getReferenceCandidates: Olympus ScanR*), which saves time for the later correlation-based referencing. The joined table is those filtered for these images only (*Reference Row Filter*).

For the Leica SP5, the Leica \*.lif container with the reference image is loaded (*Image Reader: getImages: LeicaSP5*). These images are scaled to the same pixel size as the wide-field data, rotated to the same orientation and background is subtracted (*Metanode Reference-Image-Preparation*). The position information from these images acquired with a Mark-and-Find routine in the Leica software is read (*XML Reader: getImagePositions: Leica SP5 (\*.maf)*) and cleaned (*Metanodes getPos-SP5-MarkAndFind* and *calcReferenceXYZ*).

#### 4.3 Calculating the coordinate transfer function between the two sets of reference points for each microscope and applying it on the target list

In order to relocate positions identified on a sample, a coordinate transformation between the two microscope systems (or on one microscope system after replacing the sample) needs to be performed. The point sets for calculating this transformation are obtained by mapping reference images acquired at system 2 to images within the data set acquired at system 1 by normalized cross correlation [2] (*Metanode calculateReferencePositions*; right click to configure and set pixel size). Afterwards, the tables are cleaned and sorted (*Metanodes cleanTable* and *sortReferencePoints*). In combination with the stage information, this yields the point sets in 3D space  $\mathbf{p}_1$ ,  $\mathbf{p}_2$  and  $\mathbf{p}_3$  for system 1 and  $\mathbf{p}'_1$ ,  $\mathbf{p}'_2$  and  $\mathbf{p}'_3$  for system 2, each containing a set of 3 coordinates  $\mathbf{p} = (x, y, z)^T$ . Based on these points, the connection vectors  $\mathbf{a} = \mathbf{p}_2 - \mathbf{p}_1$ ,  $\mathbf{b} = \mathbf{p}_3 - \mathbf{p}_2$ ,  $\mathbf{a}' = \mathbf{p}'_2 - \mathbf{p}'_1$  and  $\mathbf{b}' = \mathbf{p}'_3 - \mathbf{p}'_2$  are calculated. The tables containing these points are rearranged in order to use each coordinate as a KNIME flow variable (*Metanodes arrangeReferencePoints*) and joined together (*Joiner*) in one table. From both point sets,  $\mathbf{p}_1$  and  $\mathbf{p}'_1$  are also extracted as flow variables as origin points for coordinate translation. The rotation matrix is calculated the following way (*Java Snippet: rotate points*):  $\mathbf{a}$  and  $\mathbf{a}'$  are normalized to  $\mathbf{n}_1$  and  $\mathbf{n}'_1$ .  $\mathbf{n}_2$  and  $\mathbf{n}'_2$  are calculated by normalizing  $\mathbf{n}_2 = \mathbf{n}_1 \times (\mathbf{n}_1 \times \mathbf{b})$  respectively  $\mathbf{n}'_2 = \mathbf{n}'_1 \times (\mathbf{n}'_1 \times \mathbf{b}')$ . Together with the origin  $\mathbf{o} = (0, 0, 0)^T$  they describe the two normalized sets of points  $\mathbf{P}_1$  and  $\mathbf{P}_2$  in the planes, which should be rotated on one another. Their centroids are calculated  $\mathbf{c}_1 = \frac{1}{3} \sum_{i=1}^3 \mathbf{P}_1^i$  and  $\mathbf{c}_2 = \frac{1}{3} \sum_{i=1}^3 \mathbf{P}_2^i$  and used to calculate the covariance matrix  $\mathbf{H}$ :

$$\mathbf{H} = \sum_{i=1}^3 (\mathbf{P}_1^i - \mathbf{c}_1) (\mathbf{P}_2^i - \mathbf{c}_2)^T$$

which is then decomposed to its singular values

$$[\mathbf{U}, \mathbf{\Sigma}, \mathbf{V}] = \text{SVD}(\mathbf{H}).$$

The rotation matrix  $\mathbf{R}$  is calculated by

$$\mathbf{R} = \mathbf{V}\mathbf{U}^T.$$

The coordinates  $\mathbf{x} = (x, y, z)^T$  of the identified ROIs on the TMA are then transformed to system 2 by (*Java Snippet: translate points*, *Java Snippet: rotate points*, *Java Snippet: translate points*)

$$\mathbf{x}' = \mathbf{R}(\mathbf{x} - \mathbf{p}_1) + \mathbf{p}'_1.$$

#### 4.4 Generating the target list in a format readable by the microscope

For each core, a maximum of 100 ROI coordinates are selected randomly (*Group Loop Start*, *Row Sampling*, *Group Loop End*) from the transformed table. The coordinate table is brought to xml format (Metanode *setPos SP5*) and written to disk (*XML Writer*), where it can be read from the Mark-and-Find section in the Leica software controlling the confocal SP5 microscope.

## Supplementary Protocol 2

### 3D model-based image analysis quantification of subcellular structures

#### 1. 3D Gaussian model function

Subcellular structures like telomere, PML bodies and centromeres have dimensions that are close to or below the resolution of the fluorescence microscope. The apparent shape of such small spot-like structures is determined by the point-spread function (PSF) of the microscope. The PSF for 3D microscopy images can typically be well modeled by an anisotropic 3D Gaussian function [3]. Accordingly, this function is also well suited to represent the 3D intensity profile of such small spot-like structures. Using the anisotropic 3D Gaussian function

$$g_{Gaussian3D}(\mathbf{x}, \sigma_x \sigma_y \sigma_z) = \exp\left(-\frac{x^2}{2\sigma_x^2} - \frac{y^2}{2\sigma_y^2} - \frac{z^2}{2\sigma_z^2}\right)$$

where  $\mathbf{x} = (x, y, z)^T$  is a 3D position and  $\sigma_x$ ,  $\sigma_y$ , and  $\sigma_z$  are the standard deviations, the *3D Gaussian parametric intensity model* is defined as

$$g_{M,Gaussian3D}(\mathbf{x}, \mathbf{p}) = a_0 + (a_1 - a_0) g_{Gaussian3D}(\mathcal{R}(\mathbf{x}, \boldsymbol{\alpha}, \mathbf{x}_0), \sigma_x \sigma_y \sigma_z).$$

Here,  $\mathcal{R}(\mathbf{x}, \boldsymbol{\alpha}, \mathbf{x}_0)$  denotes a 3D rigid transform (e.g., [4, 5]) that comprises 3D translation parameters  $\mathbf{x}_0 = (x_0, y_0, z_0)^T$  and 3D orientation parameters  $\boldsymbol{\alpha} = (\alpha, \beta, \gamma)^T$  to represent spots with arbitrary positions and orientations, respectively. For details on the design of parametric intensity models in general see ref [5]. The parameters  $a_0$  and  $a_1$  denote the local background and peak intensity levels of the spots, respectively. The 3D ellipsoidal spot shape is given by the standard deviations  $\sigma_x$ ,  $\sigma_y$ , and  $\sigma_z$  of the model. In total, the model comprises 11 parameters  $\mathbf{p} = (a_0, a_1, \sigma_x, \sigma_y, \sigma_z, \alpha, \beta, \gamma, x_0, y_0, z_0)^T$ . The 3D Gaussian model has previously been used for quantification of 3D spot-like subcellular structures in microscopy images, for example in [3, 6-10].

#### 2. Determination of 3D subcellular structure parameters by least-squares model fitting

The spot *detection* step is conducted as described in the main text under section 2.5. For each spot identified in this manner the 3D Gaussian model  $g_{M,Gaussian3D}$  is directly fitted to the 3D image intensities  $g(\mathbf{x})$  within a spherical 3D region-of-interest (ROI). This is accomplished by minimizing the objective function

$$\chi^2(\mathbf{p}) = \sum_{\mathbf{x} \in ROI} \left( g_{M,Gaussian3D}(\mathbf{x}, \mathbf{p}) - g(\mathbf{x}) \right)^2.$$

For minimization, the iterative method of Levenberg and Marquardt (e.g., [11, 12]) was applied that incorporates first order partial derivatives of the 3D Gaussian model with respect to the model parameters  $\mathbf{p}$ . Note that partial derivatives of the image are *not* required. The partial model derivatives can be stated in analytic form:

$$\begin{aligned}
\frac{\partial g_M}{\partial a_0} &= 1 - g_{\text{Gaussian3D}}(\mathcal{R}(\mathbf{x}, \boldsymbol{\alpha}, \mathbf{x}_0), \sigma_x \sigma_y \sigma_z) \\
\frac{\partial g_M}{\partial a_1} &= g_{\text{Gaussian3D}}(\mathcal{R}(\mathbf{x}, \boldsymbol{\alpha}, \mathbf{x}_0), \sigma_x \sigma_y \sigma_z) \\
\frac{\partial g_M}{\partial \sigma_x} &= (a_1 - a_0) \frac{h_1^2}{\sigma_x^3} g_{\text{Gaussian3D}}(\mathcal{R}(\mathbf{x}, \boldsymbol{\alpha}, \mathbf{x}_0), \sigma_x \sigma_y \sigma_z) \\
&\quad \text{analogous for } \sigma_y \text{ and } \sigma_z \\
\frac{\partial g_M}{\partial \alpha} &= (a_0 - a_1) g_{\text{Gaussian3D}}(\mathcal{R}(\mathbf{x}, \boldsymbol{\alpha}, \mathbf{x}_0), \sigma_x \sigma_y \sigma_z) \\
&\quad \cdot \left( \frac{h_1}{\sigma_x^2}, \frac{h_2}{\sigma_y^2}, \frac{h_3}{\sigma_z^2} \right) \frac{\mathcal{R}(\mathbf{x}, \boldsymbol{\alpha}, \mathbf{x}_0)}{\partial \alpha} \\
&\quad \text{analogous for } \beta, \gamma, x_0, y_0, \text{ and } z_0
\end{aligned}$$

where  $(h_1, h_2, h_3)^T(\mathbf{x}, \boldsymbol{\alpha}, \mathbf{x}_0) = \mathcal{R}(\mathbf{x}, \boldsymbol{\alpha}, \mathbf{x}_0)$ . The partial derivatives of the 3D rigid transform  $\mathcal{R}(\mathbf{x}, \boldsymbol{\alpha}, \mathbf{x}_0)$  with respect to the model parameters  $\alpha, \beta, \gamma, x_0, y_0$ , and  $z_0$  have been reported previously [5]. In the procedure used here all model parameters are optimized simultaneously, except for  $\alpha$  and  $\beta$  that are kept fixed ( $\alpha = \beta = 0$ ) during optimization. The reason is that the 3D microscopy image data has a coarser voxel size in z-direction (250 nm) compared to the xy-plane (96 nm) and out-of-plane rotations have to be avoided by only enabling rotation within the xy-plane using the parameter  $\gamma$ . During iterative model fitting the minimizer might yield an invalid value for a certain parameter, e.g., a negative value for an intensity level. Such cases are automatically detected and the respective parameter is either blocked for a few iterations or its value is slightly modified (see refs [5, 13] for details). As termination criterion for the iterative minimization the relative difference between two successive values of the objective function  $\chi^2$  is used, i.e.,

$$\frac{\chi^2(\mathbf{p}_{k-1}) - \chi^2(\mathbf{p}_k)}{\chi^2(\mathbf{p}_{k-1})} < T_{\chi^2},$$

with a threshold value of  $T_{\chi^2} = 10^{-4}$ . The fitting results in estimates of all model parameters with usually subvoxel resolution. In previous studies based on nonlinear estimation theory and Cramér-Rao bounds, we have shown that for different types of 2D and 3D parametric intensity models including Gaussian models the theoretically best achievable accuracy can be reached by model fitting. Furthermore, it was demonstrated that the accuracy of the obtained 3D position and size parameters is typically in the subvoxel range [5, 14, 15].

The start parameters for model fitting are automatically determined for each detected spot candidate as follows: The 3D translation parameters  $(x_0, y_0, z_0)$  are initialized with the 3D position of the detected spot, and the 3D orientation parameters with zero, i.e.,  $\alpha = \beta = \gamma = 0$ . The peak intensity level  $a_1$  is initialized with the intensity value at the detected position, and the background intensity level  $a_0$  is initialized with the minimal intensity value within the 3D ROI used for model fitting. For the standard deviations initial values of  $\sigma_x = 1$ ,  $\sigma_y = 1.5$ , and  $\sigma_z = 2$  are chosen. The initial values are different to avoid singular matrices during iterative optimization [5].

### 3. Quantification of integrated image intensity of a given spot

Beside the quantification of individual model parameters, we also quantify the integrated intensity of each spot. In previous work the intensity of the 3D Gaussian intensity profile was integrated over the *entire* function domain, i.e., also the part of the function outside the spot



volume was considered (e.g., [7]). However, this represents only an approximation of the integrated intensity. Here, an analytic closed-form solution of the integration of the intensity over the *volume* of a spot was derived providing an exact solution. Let the spot volume  $V$  be given by an ellipsoid defined by the three standard deviations  $\sigma_x, \sigma_y, \sigma_z$  and scaled by a certain factor  $f$  in all dimensions. Then, the integrated intensity  $I$  of the spot is given by a multiplication of the spot contrast  $a = (a_1 - a_0)$  with the triple integral of the 3D Gaussian over the volume  $V$  (omitting translation and rotation w.l.o.g):

$$\begin{aligned}
I &= a \iiint_V g_{\text{Gaussian3D}}(\mathbf{x}, \sigma_x \sigma_y \sigma_z) dV \\
&= a \int_{-f \sigma_z}^{f \sigma_z} dz \int_{-f \sigma_y \sqrt{1-(z/(f \sigma_z))^2}}^{f \sigma_y \sqrt{1-(z/(f \sigma_z))^2}} dy \int_{-f \sigma_x \sqrt{1-(z/(f \sigma_z))^2-(y/(f \sigma_y))^2}}^{f \sigma_x \sqrt{1-(z/(f \sigma_z))^2-(y/(f \sigma_y))^2}} dx \exp\left(-\frac{x^2}{2\sigma_x^2} - \frac{y^2}{2\sigma_y^2} - \frac{z^2}{2\sigma_z^2}\right) \\
&\quad \text{Substitutions } x' = \frac{x}{\sigma_x} \rightarrow dx = \sigma_x dx' \text{ (analogous for } y \text{ and } z\text{):} \\
&= a \int_{-f}^{+f} dz' \sigma_z \int_{-\sqrt{f^2-z'^2}}^{+\sqrt{f^2-z'^2}} dy' \sigma_y \int_{-\sqrt{f^2-z'^2-y'^2}}^{+\sqrt{f^2-z'^2-y'^2}} dx' \sigma_x \exp(-(x'^2 + y'^2 + z'^2)/2) \\
&\quad \text{Rewriting in spherical coordinates } \varphi, \theta, r\text{:} \\
&= a \sigma_x \sigma_y \sigma_z \int_0^{2\pi} d\varphi \int_0^{\pi} d\theta \sin \theta \int_0^f dr r^2 \exp(-r^2/2) \\
&= a \sigma_x \sigma_y \sigma_z \int_0^{2\pi} d\varphi \int_0^{\pi} d\theta \sin \theta \sqrt{2\pi} \left( \frac{1}{2} \operatorname{erf}\left(\frac{f}{\sqrt{2}}\right) - \frac{f}{\sqrt{2\pi}} \exp\left(-\frac{f^2}{2}\right) \right) \\
&= a \sigma_x \sigma_y \sigma_z \sqrt{2\pi} \left( \frac{1}{2} \operatorname{erf}\left(\frac{f}{\sqrt{2}}\right) - \frac{f}{\sqrt{2\pi}} \exp\left(-\frac{f^2}{2}\right) \right) \int_0^{2\pi} 2 d\varphi \\
&= a \sigma_x \sigma_y \sigma_z 4\pi \sqrt{2\pi} \left( \frac{1}{2} \operatorname{erf}\left(\frac{f}{\sqrt{2}}\right) - \frac{f}{\sqrt{2\pi}} \exp\left(-\frac{f^2}{2}\right) \right)
\end{aligned}$$

where erf denotes the error function (e.g., [16]). Setting  $f = 1$  and using the volume  $vol = \sigma_x \sigma_y \sigma_z 4\pi/3$  of the ellipsoid, this can be rewritten as:

$$\text{integratedIntensity} = \frac{3 a \text{vol} (\sqrt{2 e \pi} \operatorname{erf}(1/\sqrt{2}) - 2)}{2\sqrt{e}}$$

## Supplementary references

- [1] C. Wählby, I.M. Sintorn, F. Erlandsson, G. Borgefors, E. Bengtsson, Combining intensity, edge and shape information for 2D and 3D segmentation of cell nuclei in tissue sections, *J Microsc* 215(Pt 1) (2004) 67-76.
- [2] B. Zitova, J. Flusser, Image registration methods: a survey, *Image Vision Comput* 21(11) (2003) 977-1000.
- [3] D. Thomann, D.R. Rines, P.K. Sorger, G. Danuser, Automatic fluorescent tag detection in 3D with super-resolution: application to the analysis of chromosome movement, *Journal of Microscopy* 208(Pt 1) (2002) 49-64.
- [4] D. Hearn, M.P. Baker, *Computer Graphics with OpenGL*, third ed., Pearson Prentice Hall, NJ/USA, 2004.
- [5] S. Wörz, *3D Parametric Intensity Models for the Localization of 3D Anatomical Point Landmarks and 3D Segmentation of Human Vessels*, Aka, Berlin, Germany, 2006.
- [6] S. Wörz, S. Heinzer, M. Weiss, K. Rohr, Model-Based Segmentation and Quantification of Subcellular Structures in 2D and 3D Fluorescent Microscopy Images, in: X.P. Hu, A.V. Clough (Eds.) *Proc. SPIE Medical Imaging 2008: Physiology, Function, and Structure from Medical Images*, SPIE Bellingham, WA/USA, San Diego, CA/USA, 2008.
- [7] S. Wörz, E. Reinz, A. Alonso, K. Rohr, 3D Model-Based Quantification of EGF Receptor Internalization from Three-Channel 3D Microscopy Images, in: K. Rohr, C. Zimmer, S. Lockett, H. Peng, J. Rittscher (Eds.) *Proc. 6th Internat. Workshop on Microscopic Image Analysis with Applications in Biology (MIAAB)*, Heidelberg, Germany, 2011.
- [8] S. Wörz, P. Sander, M. Pfannmöller, R.J. Rieker, S. Joos, G. Mechttersheimer, P. Boukamp, P. Lichter, K. Rohr, 3D Geometry-based quantification of colocalizations in multi-channel 3D microscopy images of human soft tissue tumors, *IEEE Trans. on Medical Imaging* 29 (2010) 1474-1484.
- [9] S. Osterwald, S. Wörz, J. Reymann, F. Sieckmann, K. Rohr, H. Erfle, K. Rippe, A three-dimensional colocalization RNA interference screening platform to elucidate the alternative lengthening of telomeres pathway, *Biotechnol J* 7(1) (2012) 103-16.
- [10] M. Hahn, S. Dambacher, S. Dulev, A.Y. Kuznetsova, S. Eck, S. Wörz, D. Sadic, M. Schulte, J.P. Mallm, A. Maiser, P. Debs, H. von Melchner, H. Leonhardt, L. Schermelleh, K. Rohr, K. Rippe, Z. Storchova, G. Schotta, Suv4-20h2 mediates chromatin compaction and is important for cohesin recruitment to heterochromatin, *Genes Dev* 27(8) (2013) 859-72.
- [11] D.W. Marquardt, An Algorithm for Least-Squares Estimation of Nonlinear Parameters, *Journal of the Society for Industrial and Applied Mathematics* 11(2) (1963) 431-441.
- [12] W.H. Press, S.A. Teukolsky, W.T. Vetterling, B.P. Flannery, *Numerical Recipes in C: The art of scientific computing*, Cambridge University Press, Cambridge, 1992.
- [13] S. Wörz, K. Rohr, Localization of anatomical point landmarks in 3D medical images by fitting 3D parametric intensity models, *Medical image analysis* 10(1) (2006) 41-58.
- [14] K. Rohr, Theoretical limits of localizing 3-D landmarks and features, *IEEE Trans Biomed Eng* 54(9) (2007) 1613-20.
- [15] S. Wörz, K. Rohr, Cramér-Rao Bounds for Estimating the Position and Width of 3D Tubular Structures and Analysis of Thin Structures with Application to Vascular Images, *Journal of Mathematical Imaging and Vision* 30(2) (2008) 167-180.
- [16] M. Abramowitz, I.A. Stegun, *Pocketbook of Mathematical Functions*, Verlag Harri Deutsch, Thun und Frankfurt/Main 1984.